Revision 1

Quantitative WDS Compositional Mapping Using the Electron Microprobe

John J. Donovan[1], Julien M. Allaz[2], Anette von der Handt[3], Gareth G. E. Seward[4], Owen Neill[5], Karsten Goemann[6], Julie Chouinard[1] and Paul Carpenter[7]

1. CAMCOR, University of Oregon, Eugene, Oregon, 97403, USA
2. Institute of Geochemistry and Petrology, ETH Zürich, 8092 Zürich, Switzerland
3. Department of Earth Sciences, University of Minnesota, Minneapolis, MN 55455, USA
4. Department of Earth Science, University of California Santa Barbara, Santa Barbara, CA 93101, USA
5. Department of Earth and Environmental Sciences, University of Michigan, Ann Arbor, MI 48013, USA
6. Central Science Laboratory, University of Tasmania, Hobart, Tasmania 7001, Australia
7. Department of Earth and Planetary Sciences, Washington University in St. Louis, One Brookings Drive, St. Louis, Missouri, 63130 USA

Abstract word count: 345

Abstract

While much progress has been made in electron-probe microanalysis (EPMA) to improve the accuracy of point analysis, the same level of attention has not always been applied to the quantification of wavelength-dispersive spectrometry (WDS) X-ray intensity maps at the individual pixel level. We demonstrate that the same level of rigor applied in traditional point analysis can also be applied to the quantification of pixels in X-ray intensity maps, along with additional acquisition and quantitative processing procedures to further improve accuracy, precision and mapping throughput. Accordingly, X-ray map quantification should include pixel-level corrections for WDS detector deadtime, corrections for changes in beam current (beam drift), changes in standard intensities (standard drift), high accuracy removal of background intensities, quantitative matrix corrections, quantitative correction of spectral interferences, and, if required, time dependent corrections (for beam and/or contamination sensitive materials). The purpose of quantification at the pixel level is to eliminate misinterpretation of intensity artifacts, inherent in raw X-ray intensity signals, which distort the apparent abundance of an element. Major and minor element X-ray signals can contain significant artifacts due to absorption and fluorescence effects. Trace element X-ray signals can contain significant artifacts where phases with different average atomic number produce different X-ray continuum (bremsstrahlung) intensities, or where a spectral interference, even an apparently minor one, can produce a false-positive intensity signal. The methods we propose for rigorous pixel quantification requires calibration of X-ray intensities on the instrument using standard reference materials, as we already do for point analysis, which are then used to quantify multiple X-ray maps, and thus the relative time overhead associated with such pixel by pixel quantification is small. Moreover the absolute time-overhead associated with this method is usually less than that required for quantification using manual calibration curve methods, while resulting in significantly better

accuracy. Applications to geological, synthetic, or engineering materials are numerous as quantitative maps not only show compositional 2D variation of fine-grained or finely zoned structures, but also provide very accurate quantitative analysis, with precision approaching that of a single point analysis, when multiple-pixel averaging in compositionally homogeneous domains is utilized.

Keywords: EPMA, WDS, quantitative analysis, X-ray mapping, quantitative mapping.

Introduction

Quantification of WDS X-ray intensities by electron-probe micro analysis (EPMA) has progressed over the last few decades with the development of better instrument hardware for stable operation, and improved software for physics-based background, matrix, and spectral interference corrections (Armstrong, 1988; Donovan et al., 1993; Donovan and Tingle, 1996). However, these advances have generally been limited to so-called “point analysis”, by which we mean quantitative characterization of elemental chemistry, typically at a nominal volume of a cubic micrometer, when the beam and stage are stationary with respect to each other. This quantitative point analysis now approaches and may be better than 2% relative accuracy for major and even minor elemental concentrations in many compositional matrices. Additionally, these improvements in both hardware and software, combined with measurements at high beam currents and extended integration times, have demonstrated sensitivity at ppm levels for quantitative point analysis in selected materials (e.g., Donovan et al., 2011; Batanova et al., 2015).

In practice, quantitative EPMA point analysis can be performed in minutes for a suite of elements and includes both background and matrix corrections. Conversely, X-ray maps obtain spatial information by limiting the dwell-time per pixel to hundreds to thousands of milliseconds, which, depending on the pixel resolution and sensitivity required, can take hours to days of map acquisition time. These shorter pixel intensity integration times result in a reduction in precision due to counting statistics, but in principle it does not reduce accuracy when the pixel intensity values are corrected using the same methods that are already utilized for conventional point analysis.

Some investigators have proposed using calibration curves for quantification of raw intensity X-ray maps and such alternative quantification methods will be discussed below. However, except for specialized circumstances (e.g., trace carbon in steel [Eichen et al., 1972]; low voltage analysis [Moy at al., 2020]), such methods are problematic for optimal accuracy, especially in multi-phase materials often encountered by geologists and material scientists.

It should be noted that the evaluation of raw X-ray intensity maps may be no better than comparing raw intensities from point measurements, if the map interpretation is dependent on quantitative comparisons, as is usually the case. Analysts do not generally compare raw X-ray count rates when interpreting their point analyses, as these count rates include the bremsstrahlung ("background" or continuum X-ray signal) and are also subject to non-systematic variations due to matrix effects; likewise, count rates obtained during X-ray mapping are subject to these same effects, and therefore evaluation of raw intensity X-ray maps are subject to the same pitfalls (i.e., the same X-ray intensity can represent widely different concentrations from pixel to pixel depending on the composition of the specific pixel under examination). Science depends on accurate numerical quantification and X-ray mapping should be no exception. This

paper describes a quantification protocol for the treatment of WDS element X-ray maps obtained on the electron microprobe, in order to yield the most accurate and precise results, just as we already do for our point analyses.

Acquisition of X-ray Maps for Quantification Using the Electron Microprobe

X-ray element mapping can be performed either using a wavelength-dispersive spectrometer (WDS) or a silicon-drift energy dispersive spectrometer (EDS) with pros and cons for each detector. Modern silicon-drift EDS systems exhibit high throughput of X-ray intensities and can be important for element mapping of major elements. The main advantage of EDS is to measure simultaneously a wide range of X-ray energies during acquisition in a relatively short amount of time, i.e. a few seconds per point, though artifacts in EDS spectra (see below) can become problematic at typical high beam currents necessary for efficient mapping. Unfortunately, when scanning over large areas and collecting X-rays as pixels, the counting statistics on a given pixel at a given energy channel are comparatively poor, and therefore the peak-to-background (P/B) ratios remain low. Moreover, EDS systems often exhibit high dead times at the elevated beam current values typically used for element mapping of minor and trace elements (>100-200 nA). At such high beam currents, these tradeoffs result in utilizing either a shorter pulse processing time constant at the cost of poorer spectral resolution, which is not ideal for quantification, or a longer pulse processing time constant by utilizing a reduced EDS-aperture size, which reduces sensitivity and introduces spectral artifacts. Furthermore, the development of pileup peaks and Si-escape peaks (Newbury, 1995) complicates the quantitative analysis and interference

correction of EDS spectra, although new EDS algorithms may offer better corrections for these artifacts (Newbury and Ritchie, 2019).

Measurement by WDS has the superior advantages of higher P/B and X-ray counting rates as the X-ray wavelength of interest is selected by Bragg diffraction, and the counting electronics process only these selected pulses and automatically rejects most high-order X-ray line reflections, when differential pulse height analysis (PHA) parameters are properly adjusted. These improved WDS P/B statistics and higher counting rates result in better analytical sensitivity, and they allow WDS to be used not only for major, but also for minor and trace element measurement. WDS is also the preferred choice for routine analysis and element mapping of a wide range of phases, and excels in the measurement of elements at trace element concentration and/or having low energy X-rays. (Goldstein, et al., 1992). In this paper we will limit ourselves to a discussion of quantitative analysis of WDS X-ray maps acquired with EPMA instruments.

Element mapping by WDS on the electron microprobe is usually performed by using a fixed electron beam ("spot" mode) in combination with specimen stage scanning motion, an approach referred to as "stage mapping". This fixed beam is used to avoid lateral defocusing of the spectrometer when scanning sample areas larger than the WDS Bragg focus dimension. During stage mapping, the image pixel dimension is defined by the stage motor step size, and the electron beam diameter is usually set equal to or slightly less than this pixel dimension. On JEOL microprobes the stage sample holder is then scanned in y-axis strips with incremental movement of the x-axis starting on the top-right corner, and on Cameca microprobes the stage is scanned in x-axis strips with incremental movement of the y-axis starting on the top-left corner. These differences have implications for how the calculations for beam drift and standard intensity drift

corrections are applied to the pixel acquisition order. It should also be noted that when stage maps are acquired over large sample areas or for long durations, both the flatness of the sample and the stability of the instrument are of paramount importance for X-ray map quantification. Any changes in the sample Z-axis focus or instrument stability can result in significant X-ray measurement errors due to changes in Bragg defocus and column and/or spectrometer alignment.

For higher spatial resolution, a beam scanning method with sub-micron pixel size is preferred in order to minimize stage reproducibility errors after each pixel strip and between multiple passes over the same area. This beam mapping method can only be performed on small areas, where Bragg defocusing effects are negligible (< 20-40 μm lateral map dimensions, dependent on the WDS Rowland circle and the specific Bragg crystal). In either case, each pixel records the total X-ray count on each WDS channel, with each spectrometer tuned to an X-ray characteristic peak position of an element of interest. For multiphase samples with numerous major and minor elements to map, it is typically necessary to perform this acquisition using 1 to 3 or more passes over the same sample area; one pass for each set of WDS elements to be measured. For instance, on a 5-spectrometer microprobe it is necessary to do 2 passes of 5 elements each to acquire up to 10 elements for a typical silicate analysis (usually Si, Al, Fe, Mn, Mg, Ca, Na, and K, and as required Ti, Cr, P, S, Ni or other trace or minor elements of interest).

For accurate map quantification, it is necessary to remove any intensities not pertaining to the characteristic X-ray to be quantified. First and foremost is the bremsstrahlung, which is commonly referred to as the X-ray continuum or X-ray background. The conventional background correction method for point analysis is to drive the WDS spectrometer to two off-peak positions, that is, to the sides of the characteristic X-ray peak position, in order to measure the X-ray intensity at a spectrometer position where only continuum X-rays satisfy Bragg's law.

By extrapolating or interpolating such intensity values to the on-peak position, the continuum intensity under the peak can subsequently be determined. Such off-peak background measurements can also be acquired during quantitative X-ray mapping, but this requires the acquisition of not only an on-peak map, but also the additional acquisition of at least one (e.g., Cameca PeakSight software, https://www.cameca.com/), and ideally two background maps (Probe Software Probe Image software, https://probesoftware.com/), particularly for emission lines where the continuum spectrum is highly sloped or curved (e.g., at low spectrometer limits; Jercinovic et al., 2012). If two background X-ray maps are acquired, an interpolation of the intensities is made at each pixel using linear, polynomial, exponential or slope regression methods in order to obtain the background intensity to subtract from the on-peak X-ray map pixel intensity.

However, considerable acquisition time can be saved if no background X-ray maps are actually acquired, but rather the background intensity is constrained by a standards-based background calibration curve such as the mean atomic number (MAN) background correction method (Kramers, 1923; Merlet and Bodinier, 1989; Donovan and Tingle, 1996). The use of the MAN background corrections do not require the acquisition of off-peak X-ray maps at all, thus resulting in not only significant savings in mapping acquisition time, but also improved sensitivity due to the statistics of the MAN background correction method (Donovan et al., 2016). This approach is recommended and discussed further below.

Calibration Curve and Other Methods for X-ray Map Quantification

Tinkham and Ghent (2005) have proposed X-ray map pixel quantification using Bence-Albee (hyperbolic) calibration curve methods, combined with a single standard MAN background correction, which they claim can produce quantitative X-ray maps, except in cases of high absorption or fluorescence (Donovan, et al., 2019), or when mapping trace elements in multi-phase materials with different average atomic numbers (see below for more details). However, since we already have more accurate analytical physics and background removal techniques available from point analysis methods, it is reasonable to apply our full knowledge of electron-microprobe physics to the analytical situation at hand, whether that application is point analysis or X-ray mapping.

Alternatively, some investigators (e.g., Lanari et al., 2014; Ortolano et al., 2018) have proposed quantifying raw X-ray maps by means of calibration curve methods. These methods attempt to relate the raw X-ray intensities in maps to concentrations determined from at least two or more single-point analyses that are considered representative of the range of compositions of the different phases within the map area. From this, one can interpolate concentrations for a given arbitrary X-ray intensity. Although in principle this method appears to provide some usefulness for quantification of X-ray maps of a single phase, the nature of electron and X-ray physics informs us that when applied to situations with multiple phases, each with diverse matrix physics, these assumptions of compositional linearity are unfounded (Barkman et al., 2013, Donovan et al., 2019). Even worse are these assumptions, applied to trace minor and element analysis, when multiple phases with different average atomic numbers are present, as each zero concentration is represented by a different X-ray intensity. The calibration curve method is also unable to accurately correct for spectral peak interferences in different phases.

In systems with multiple phases, the same X-ray intensity in different phases can represent quite different elemental concentrations due to absorption and/or fluorescence effects. Similarly, the X-ray intensity corresponding to a zero concentration of an element, i.e., the bremsstrahlung intensity at the peak position of interest, depends wholly on X-ray continuum absorption and on the average atomic number of the phase, which can vary significantly from one phase to another and sometimes even within one a single phase exhibiting substantial compositional zonation. For example, Si Kα intensity data obtained in multiple silicate reference materials plotted against the Si concentration do not lie on a linear line trend, and even an exponential calibration curve cannot be properly fitted (Fig. 1).

Due to differences in the matrix correction physics for each of the phases plotted, there is insufficient linearity to robustly correlate intensity to concentration when more than a single phase is present or when a strong compositional zonation is observed and is not fully covered by the single-point analysis obtained in the phase of interest. It is in fact, precisely for this reason that such calibration curves are very limited in application for EPMA point analysis quantification, with rare exceptions such as trace carbon in steel, where several reference materials of similar range in composition are considered (Crisci et al., 2006). These non-linearities are even more obvious when examining the numerical results from a generic multi-standard calibration curve as seen in Table 1 for the analysis of several different standard materials. Clearly, we should expect better accuracy than this for our X-ray map quantification efforts.

A New Method for Rigorous Quantification of X-ray Maps

The method for quantitative X-ray mapping presented in this paper largely replicates the quantitative methods already developed for point analysis. The main difference is that the full set of correction algorithms are applied to intensities measured at each individual pixel in the X-ray map, rather than just a single discrete point. This process, summarized in Figure 2 and detailed in the following discussion, begins with the extraction of the array of raw counts obtained for all elements on each pixel, one pixel at a time. The counts received are normalized to the counting time and beam current to yield X-ray intensities in counts per second per nanoamp (cps/nA). These resulting intensities are then corrected for dead time, beam drift, standard intensity drift, background, and time dependent intensity (TDI) corrections when necessary, e.g. for beam sensitive samples and for contamination issues such as trace carbon measurements. This whole correction procedure is then run iteratively through a full matrix correction, either ZAF or $\phi(\rho z)$ methods, as required by the analyst, along with any quantitative spectral interference corrections specified by the user. Of course, the exact same normalization and correction procedures are also applied to the standard intensities from point measurements, which will be utilized not only in the construction of the intensity k-ratio prior to the matrix correction procedures, but also in the calculation of the MAN (absorption corrected) background calibration curve for each analyzed element, and in the peak interference correction (if necessary) for the primary standards.

Intensity Normalization and Dead Time Correction

The first step in the quantification of X-ray maps is to divide the total X-ray intensities in both the standard point measurements and the unknown pixel measurements, by their respective integration times and beam currents to obtain counts per second per nanoamp (cps/nA) intensities (equation 1).

This is the peer-reviewed, final accepted version for American Mineralogist, published by the Mineralogical Society of America.
The published version is subject to change. Cite as Authors (Year) Title. American Mineralogist, in press.
DOI: https://doi.org/10.2138/am-2021-7739. http://www.minsocam.org/

$$i_{cps/nA} = \frac{i_{counts}}{t*nA} \quad \text{(Eq. 1)}$$

Where :

$i_{cps/nA}$	Normalized intensity in counts per second per nanoamp
i_{counts}	Number of total raw X-ray intensity measured
t	Counting integration time in seconds
nA	Beam current in nanoamps (measured or interpolated)

The beam current values utilized for the standards are the measured beam currents from the standard intensity point measurements, while the beam current values for the map pixels are the interpolated beam currents measured prior and subsequently to the pixel intensity mapping measurements (see below for details).

Second, a dead time correction is applied using a single factorial expression (equation 2a). However, when utilizing high beam currents to improve sensitivity, the count rate can exceed 50,000 counts per second, and a high-precision expression that extends the factorial to another term is usually preferred (equation 2b).

$$i_{dt} = \frac{i_{cps}}{1-i_{cps}*\tau} \quad \text{(Eq. 2a)}$$

$$i_{dt} = \frac{i_{cps}}{1-\left(i_{cps}*\tau+\frac{\tau^2}{2}\right)} \quad \text{(Eq. 2b)}$$

Where :

i_{dt}	Dead time corrected intensity

This is the peer-reviewed, final accepted version for American Mineralogist, published by the Mineralogical Society of America.
The published version is subject to change. Cite as Authors (Year) Title. American Mineralogist, in press.
DOI: https://doi.org/10.2138/am-2021-7739. http://www.minsocam.org/

261 τ Dead time constant in seconds

262 i_{cps} Intensity in cps

263

264 ***Correction for Beam Drift and Standard Drift***

265 Corrections for drift of the electron beam current are generally applied to the quantification of X-
266 ray maps due to the frequently extended acquisition times, even for modern instruments with
267 beam current regulation. This beam drift correction is usually based on the beam current
268 measurement before and after each map acquisition, and is normalized to the X-ray intensities
269 for each pixel based on the elapsed time between these beam current measurements. See
270 equation 3, which assumes the (slow) increment step motion is in the y-axis direction. Other
271 beam drift correction methods include measuring the beam current before and after each scan
272 line, though this procedure may not be necessary in modern instruments when the total map
273 acquisition time is less than 10 or 20 hours.

274 $$nA_{Interpolated} = nA_{Start} + (nA_{End} - nA_{Start}) * \frac{(P_x + (P_y - 1) * P_x)}{(N_x * N_y)} \quad \text{(Eq. 3)}$$

275 Where :

276 $nA_{Interpolated}$ Interpolated mapping beam current

277 nA_{Start} Starting mapping beam current

278 nA_{End} Ending mapping beam current

279 P_x Position of a pixel the x array dimension

This is the peer-reviewed, final accepted version for American Mineralogist, published by the Mineralogical Society of America.
The published version is subject to change. Cite as Authors (Year) Title. American Mineralogist, in press.
DOI: https://doi.org/10.2138/am-2021-7739. http://www.minsocam.org/

280 P_y Position of a pixel the y array dimension

281 N_x Number of pixels in the x array dimension

282 N_y Number of pixels in the y array dimension

283 Similarly, if standard intensities were measured before and after the X-ray map acquisition, a
284 drift correction in the standard intensities can be applied (equation 4). This drift corrected
285 standard intensity is calculated on an element by element basis for each pixel and is applied to
286 the denominator of the k-ratio prior to the quantitative matrix correction.

287 $$I_s = I'_S + (I''_S - I'_S)\frac{(T_P - T'_S)}{(T''_S - T'_S)} \quad \text{(Eq. 4)}$$

288 Where :

289 I_s Interpolated (drift corrected) standard intensity

290 I'_S Standard intensity from the preceding standardization

291 I''_S Standard intensity from the following standardization

292 T_P Acquisition clock time of the X-ray map pixel

293 T'_S Acquisition clock time of the preceding standardization

294 T''_S Acquisition clock time of the following standardization

295 Both the beam drift and standard intensity drift corrections assume linear drift in between beam
296 current and standard intensity measurements, and of course are also dependent on the pixel
297 acquisition order which depends on the map acquisition (slow) step increment direction, and the
298 instrument vendor as previously discussed.

299

300 ***Aggregate Intensities for Duplicate Elements***

301 Sometimes we need to improve the geometric efficiency of our photon collection by measuring
302 the same element on multiple WDS spectrometers simultaneously (Donovan et al., 2011).
303 Different spectrometer/crystal combinations can be used as long as the same X-ray line emission
304 is utilized for each duplicate element. By aggregating intensities from several spectrometers, the
305 analytical sensitivity and thus the detection limit can be significantly improved. The intensities
306 for both the standard and the unknown are aggregated prior to the construction of the elemental
307 k-ratio (see section Trace Elements and Spectrometer Aggregation below for details).

308

309 ***Correction for X-ray Continuum***

310 WDS background (i.e., X-ray continuum) measurement is central to accurate quantitative
311 microanalysis, especially for minor and trace elements. As mentioned previously, one or two
312 background maps can be acquired to subtract the interpolated background from the on-peak map
313 pixels, at the cost of at least doubling the total mapping time. Alternatively, the mean atomic
314 number (MAN) background method offers another background calibration method and provides
315 a number of benefits for microanalysis, especially with regards to acquisition time and precision,
316 particularly for X-ray mapping. Some investigators (Tinkham and Ghent, 2005), have utilized a
317 single MAN standard for X-ray map background corrections, but this is insufficiently accurate
318 for maps containing multiple phases with different average atomic numbers. However, by
319 measuring the X-ray intensity at the characteristic peak position for a given element on multiple
320 standards (that do not contain the element), and which includes the range of average atomic

number for the unknown phases to be mapped, we can create a robust relationship between these continuum intensities and average atomic number of these standards. Such MAN standard plots, usually acquired during the primary standard intensity calibration, yield an accurate WDS background calibration, provided that a correction for continuum absorption is properly applied to the measured intensities for each standard (Donovan et al., 2016).

The X-ray intensity data collected for these MAN plots are generally acquired at the same conditions as any other standard acquisition, and therefore have a precision that is equal to that for conventional spot analysis. For compositional mapping applications, the MAN background correction also provides an accurate background calibration that is used for all pixels in the map and at a precision that is superior to the counting statistics of conventional "off-peak" acquired background maps. In most silicate and oxide materials, the absolute accuracy of the MAN background correction is typically around 200 to 300 ppm, which is usually smaller than the expected precision of most X-ray map pixel intensities. The greatest benefit of the MAN background method is that all counting time in the mapping run is dedicated to measurement of the characteristic X-ray peak, which significantly improves the precision and detection limit of the element (Donovan et al, 2016). Since the MAN method is more time efficient and actually provides better sensitivity, it is generally the preferred method for background correction of X-ray maps. Although MAN background calibrations might be slightly less accurate than using off-peak maps for background corrections, for example when phases contain unanalyzed (or unspecified) elements such CO_2 in carbonates (depending on the details of the differences in average atomic number), utilizing MAN background corrected X-ray maps does reduce the necessity for repeated map acquisitions, thus also reducing concerns regarding stage reproducibility and instrument stability. In addition, accuracy is further improved because the

MAN background method completely avoids the problem of spectral interferences on off-peak intensity measurements from other emission lines, since these off-peak intensities are no longer acquired when utilizing the MAN method. Finally, if necessary, a blank correction (Donovan et al., 2011) can be applied to the X-ray maps, if the map matrix is suitable, for even better accuracy.

Correction of Spectral Interferences

Correction of spectral interferences are applied to the pixel on-peak intensities during the matrix correction iteration based on the concentrations of the interfering elements (Donovan et al., 1993). This correction must be done iteratively with the matrix correction (Fig. 2; equation 5) as the interference correction can change the composition of the pixel significantly enough so that the matrix correction must be re-calculated based on the newly re-calculated concentrations of all elements; this is even more important when considering mutual interferences of two analyzed X-rays (e.g., Ti Kβ interferes with V Kα, and V Kβ interferes with the trace levels of Cr Kα in Al-Ti-V-Cr alloy).

$$C_A^u = \frac{C_A^s}{[ZAF]_{\lambda_A}^s} [ZAF]_{\lambda_A}^u \frac{I^u(\lambda_A) - \frac{[ZAF]_{\lambda_A}^{\bar{s}}}{C_B^{\bar{s}}} \frac{C_B^u}{[ZAF]_{\lambda_A}^u} I_B^{\bar{s}}(\lambda_A)}{I_A^s(\lambda_A)} \quad \text{(Eq. 5)}$$

Where:

C_i^j Concentration of element i (A = measured element; B = interference element) in matrix j

This is the peer-reviewed, final accepted version for American Mineralogist, published by the Mineralogical Society of America.
The published version is subject to change. Cite as Authors (Year) Title. American Mineralogist, in press.
DOI: https://doi.org/10.2138/am-2021-7739. http://www.minsocam.org/

363 $[ZAF]^{j}_{\lambda_i}$ ZAF or $\phi(\rho z)$ correction term for matrix j at λ_i for element i

364 $I^{j}_{i}(\lambda_i)$ Measured X-ray intensity in matrix j at wavelength λ_i

365 u Unknown sample which contains elements A and B

366 s Primary standard which contains only element A

367 $\bar{s}$ Interference standard which contains a known quantity of the interfering
368 element B, but none of the interfered with element A.

369

370 When necessary, this quantitative spectral interference correction routine is applied to each pixel
371 of the acquired maps (and the standard point analysis intensities also), providing of course that
372 the X-ray intensities of both the measured and the interfering elements are available.

373

374 ***Correction of Time Dependent Intensity Effects***

375 Correction of time dependent intensity (TDI) effects, such as alkali-migration in glasses due to
376 beam damage (cf. Nielsen and Sigurdsson, 1981; Morgan et al, 1996), is quite straight forward
377 for point analysis, as it simply requires acquisition of "sub-interval" intensities during the on-
378 peak measurement to monitor and correct for change in count rate over time. The same principle
379 can be applied on beam mapping: by acquiring multiple frames of X-ray maps, we can obtain an
380 evolution of the count rate for each pixel over time, and thus correct for possible changes in X-
381 ray intensity by extrapolating back to the intensity at time zero using equation 6.

382
$$I_C = e^{Log(I_R) - m \cdot t \cdot 0.5} \quad \text{(Eq. 6)}$$

Where:

I_R	X-ray intensity in counts per second per nA
m	Time Dependent Intensity (TDI) slope coefficient from linear fit of log intensity versus time
t	Total elapsed integration time

Linear, quadratic, or logarithmic TDI fitting models can be applied on an element-by-element basis; quadratic or logarithmic corrections are often necessary for extremely beam sensitive materials (von der Handt, in preparation).

Correction of Compositional Matrix Effects

Once the k-ratios for each element are calculated from the normalized and background corrected unknown map pixel and standard point intensities, a matrix correction can be applied. Selection of the proper matrix correction routine is out of the scope of this paper and the analyst will be the judge of that choice. Typical analytical physics models can be used (e.g., ZAF or $\phi(\rho z)$) or even Monte Carlo methods (Donovan, 2019). In general, quantitative analysis using the electron microprobe is generally based on equation 7:

$$C = k * [ZAF] \quad \text{(Eq. 7)}$$

Where C is the concentration result, [ZAF] is the total matrix correction, including the standard k-factor correction for when the standard is not a pure element (e.g., Armstrong, 1988), and k is the raw k-ratio intensity expressed as $(I)^{sample} / (I)^{standard}$, where I are the continuum corrected

peak X-ray intensities measured on samples and standards respectively. Modern matrix correction algorithms correct for electron energy-loss and backscattering in the atomic number factor Z, absorption of characteristic X-ray intensities in the absorption factor A (both which are combined in $\phi(\rho z)$ matrix correction methods), and additional X-ray intensities resulting from characteristic (and ideally continuum) X-ray fluorescence in the fluorescence factor F. This matrix correction is made iteratively using a refined estimate of the pixel concentration. The final analysis result is identified when no further improvement in the concentrations is obtained, just as in the case of single point analysis. In fact we utilize the same source code for both point analysis and map pixel analysis in all our results.

Additional Corrections for Soft X-rays

Not discussed in this paper are the effects of changes in peak shape on soft X-rays and the correction algorithm using area peak factors (Bastin and Heijligers, 1991). This approach is applied for the accurate quantification of low atomic number emitters. However, due to the chemical bonding dependency of such corrections, they are of limited use in X-ray mapping when multiple phases are present. Nonetheless, it should be mentioned that the choice of different matrix correction models and mass absorption coefficients can have significant effects on the accuracy of quantitative results and should be considered when performing quantitative X-ray mapping with highly absorbed emission lines, such as low atomic number K-lines or other very soft X-ray emission lines, e.g., L-lines of first row transition elements.

Computation Time and Complementary Calculations

The processing of a typical set of 10 element X-ray maps of 512 x 512 pixels will require tens of minutes to a couple hours of matrix physics calculation time depending on the speed of the computer; most modern computers will process the data of smaller maps with fewer elements in less than 10 minutes. Elemental concentrations, along with background-, net-, and k-ratio intensities are generally calculated by default. An analytical total weight percent map is also usually calculated to further help in judging the data quality. In addition, other information can be mathematically extracted from the elemental concentration data, such as oxide weight-percent, atomic proportions, formula basis calculations, and logarithmic weight-% of concentrations for trace element mapping. Statistical data such as detection limits and analytical sensitivities can also be calculated for each pixel as well. Optionally, and if appropriate for the compositions in question, several other map data can be extracted, such as a stoichiometric oxygen map, an excess oxygen map (from assumed oxygen stoichiometry and/or measured anions such as F and Cl), and a map of an element calculated by difference from 100%. To facilitate the calculation of all specified output types it is more efficient to calculate them during the map quantification, although they can be easily recalculated using the primary output (elemental weight-%).

Because all pixels during the quantification of X-ray maps are treated to the same matrix correction methods as we traditionally perform for point analyses, very large maps with many elements can require considerable time for the calculation of concentrations. The calculation-time scales linearly with the number of pixels and exponentially with the number of elements analyzed. The fully automated processing of these quantitative maps can be done off-line on any computer without any action from the user besides the selection of the appropriate quantification

parameters (e.g., choice of primary and interference standards, definition of the MAN background curves, calculated elements [by stoichiometry, by difference, etc.]). All maps presented in this paper follow the procedures as presented above and were performed using the Probe Software Probe for EPMA and CalcImage software packages (https://probesoftware.com/), though other software codes could perform similar quantitative corrections to raw X-ray map intensity data.

Results and Discussions

Primary standards required for quantitative mapping are usually acquired as point analyses at a moderate beam current (typically 10-50 nA) with integration times of 10-30 s. However, stage or beam scanned X-rays maps are usually acquired at higher currents, typically 20 to 500 nA, even 1 μA in cases of trace element mapping, and using a pixel dwell time on the order of tens to hundreds of milliseconds or more per pixel (which makes it essential that the actual beam currents be recorded for both the standards and the X-ray map acquisitions in real-time). Since both time and beam current should scale proportionally, doubling the count time is equivalent to doubling the beam current (ignoring dead time effects). To compare data and evaluate the precision of each measurement, the total electron dose (i.e., the product of beam current and time) should be considered. Ignoring the effects of electron beam energy in beam power calculations, we can simply say that single point analyses, for instance in standards, typically yield a total electron dose in the range of 100 to 3000 nA·s. Quantitative element maps runs typically utilize higher currents (20-500 nA) to compensate for shorter count times (20-1000 ms), which translate to a dose range of 0.4 to 500 nA·s per pixel. In other words, even well-chosen

conditions for element maps can still represent an electron dose several orders of magnitude less than for single-point quantitative analysis. This dose should be carefully considered with regards to the beam size, and the applied dose should be normalized to the impacted surface (i.e., expressed as $nA \cdot s/\mu m^2$). This calculation of electron dose is useful for evaluating the precision and detection limit for conventional single-point versus map-pixel analysis and reveals that mapping measurements have usually lower precision and therefore higher detection limits at each individual pixel (Carpenter et al., 2017). It is therefore legitimate to ask how precise and accurate quantitative element mapping truly is. Calculation of the electron dose can also be useful to evaluate the maximum allowable dose for beam sensitive materials before beam exposure damages the sample too much, resulting in inaccurate results. In such cases, large area stage mapping is often done with a relatively large beam size that matches the pixel size to further help dissipating the electron dose over a large area, thus minimizing the problem of beam damage.

Evaluation of Accuracy

It is not immediately obvious that X-ray maps acquired using a dwell time per pixel of a few hundred milliseconds or even less, can be accurately quantified due to the apparently poor counting statistics per pixel. But accuracy depends primarily on matrix corrections, background and peak interference corrections, standard reference values, etc. All these parameters remain the same whether a single-spot analysis or quantitative element map pixel is considered, and therefore the map-derived element concentrations should be just as accurate as a single point measurement, with the caveat that the absolute accuracy of the pixel dwell times (for both

492 "continuous" and "step" mapping modes) at the millisecond level should be verified by both the
493 instrument vendor and user, for best quantitative mapping accuracy. In addition, when the
494 primary standards and X-ray maps are acquired at significantly different beam currents, the
495 linearity of the beam current picoammeter is critical for best accuracy, not to mention the
496 importance of the WDS detector dead time calibrations when high X-ray intensities from high
497 mapping currents are combined with standard intensities acquired with lower beam currents for
498 the primary standard calibrations, in the subsequent construction of the raw k-ratio prior to
499 quantification.

500 In any case, all quantitative measurements require an average and a variance regardless of
501 whether this is for point or pixel measurements. Similar to point analyses, a representative
502 sampling of the specimen composition requires the examination of an average and standard
503 deviation of each set of points or of pixels, especially in multi-phase materials.

504 To demonstrate the accuracy of the proposed quantitative mapping approach, a simple X-ray
505 map in the reference glass material NIST K-411 is quantified (Fig. 3). For this example, element
506 maps were acquired using a Cameca SX-100 electron probe microanalyzer at CAMCOR
507 (University of Oregon), using analyzing crystals LIF for Fe Kα, PET for Si Kα, LPET for Ca
508 Kα, TAP for Al Kα, and LTAP for Mg Kα. Analytical conditions were 15 keV, 30 nA using a
509 128 x 128 pixels stage scan with a pixel dwell time of 500 ms and a pixel size of 0.5 µm. Results
510 of the quantification process are given in Figure 3. In this map quantification, oxygen was
511 calculated by stoichiometry with an additional 1.12 wt% oxygen from ferric iron (as determined
512 from colorimetry). All maps are corrected for background using the MAN background
513 correction. The calculation of a total concentrations map (g) provides for evaluation of the
514 analysis accuracy as all elements should total close to 100%. The calculated quantitative pixel

515 average results are subsequently compared to NIST published values (Table 2). Excellent
516 accuracy is achieved as the calculated weight-% of all four major elements (Si, Mg, Ca, and Fe)
517 are statistically equivalent to the certified NIST values, and Al accurately yields a zero-value
518 (nominally Al-free glass).

519

520 ***Evaluation of Precision***

521 The shorter pixel integration times of X-ray mapping compared to point analysis generally leads
522 to poorer Poisson statistics. Therefore, the apparent precision per pixel is more limited, and it
523 should be evaluated carefully. Mapping precision and sensitivity are considerably improved by
524 pixel averaging, as it is commonly done for multiple point measurements in a homogeneous area
525 or by kernelling or binning such as it is already done for instance with EDS maps. Such pixel
526 averaging can provide enough precision for discriminating small differences in concentrations
527 and can ultimately increase the analytical sensitivity.

528 Table 3 compares point analyses (average of 4 points) of standard material NIST K-411, with
529 pixel averages from the quantitative X-ray map (Fig. 3), using pixel aggregates from 4 to 64
530 pixels. Comparing pixel averages with point averages reveals that accuracy and standard
531 deviation (pixel variance) are consistent and in close agreement with the average and variance of
532 4-point averaged measurements. Naturally, the error of the mean or standard error (pixel error),
533 improves significantly with the number of pixels being averaged (Table 3).

534

Bad Pixels

When considering pixel averaging in an unknown sample we must also consider the adverse effects from so-called "bad pixels" that can degrade our quantitative maps with inaccurate data. A bad pixel is often the consequence of breaking one of the essential requirements of WDS measurement (flat and horizontal surface, homogeneous domain, proper working distance, etc.) or a hardware issue (e.g., sudden beam current instability, noise on a WDS X-ray detector, etc.). Excluding hardware problems, a typical bad pixel is commonly due to surface defects (holes, cracks, poor polishing, etc.), phase boundaries (Barkman et al., 2013), or finely intergrown materials or exsolutions. The choice of beam diameter and accelerating voltage along with the density of the analyzed phase will control the size of the analyzed volume. When a larger analytical volume is considered, a higher number of bad pixels is to be expected, especially when the average grain-size or feature to be mapped is approaching the size of the analytical volume. In other words, the larger the analytical volume and/or the smaller the phase dimensions, the greater the number of pixels compromised by edge, crack and mixed-phase interaction volumes. Large well-polished phenocrysts might give overall excellent results, but a fine-grained heterogenous matrix may not. For this reason, the best approach would utilize a focused beam, despite the fact that this would increase the current density and potential for beam damage. The key point is to constrain the analytical volume and the pixel size to ultimately obtain a representative number of pixels for the smallest feature to be mapped while minimizing the number of bad pixels.

When considering pixel averaging, including “bad pixels” in the average can affect both the precision and the accuracy. Therefore, the use of pixel extraction and filtering methods are recommended and available in many image processing programs (e.g., Probe Software

CalcImage, NIH ImageJ, etc.). This approach allows the analyst to specify the exact pixel area to be extracted from the map by providing for instance, a pixel filtering based on quantitative compositional limits for selected analyzed elements. In this way one can avoid and/or filter out these bad pixels from our compositional averages. An example is provided later in this paper.

Quantitative Mapping Results

Geologists and materials engineers commonly require detailed element mapping of complexly zoned phases. Whereas point analysis yields very precise and accurate data, it commonly fails at revealing all the subtleties of compositional zonation (if present). Mapping is therefore necessary, and as discussed above, both precision and accuracy can be obtained depending on the analytical settings and the pixel averaging employed.

As a first example, a simple mapping of plagioclase with 5 major elements (Si, Al, Ca, Na, and K) is considered. The sample is from the Adamello tonalite in Northern Italy (Fiedrich et al., 2017), and shows strong compositional zoning from an inherited anorthite-rich core to an albite-rich rim overgrowth showing a significant oscillatory zoning. After performing the quantitative calculations for each pixel, the fully quantitative elemental or oxide weight-percent (wt%) concentrations are available for output (Fig. 4a). In addition, these elemental concentrations can be expressed in any number of various output types, such as atomic percent or formula basis (Fig. 4b), and various end-member mineral normalizations. Additional normalizations based on the previously calculated elemental or molar concentrations can also be performed. For example, mineral end-member calculations where the Ca, Na, and K concentrations are normalized to produce maps of anorthite, albite, and orthoclase end-member components for each pixel in the

original map (Fig. 4c), though multiple normalizations may be necessary when more than one mineral phase is present.

If a single-phase is of interest to the researcher, pixel filtering and extraction based on chemical composition and the analytical total can be applied. In Figure 4d, only the pixels corresponding to a plagioclase composition are extracted; the conditions in this example are: 90% < Total < 110 wt%, 40 < SiO_2 < 75 wt%, 15 < Al_2O_3 < 40 wt%, CaO < 25 wt%, Na_2O < 15 wt%, and K_2O < 2 wt%. This compositional filtering also allows us to remove any of the previously discussed bad pixel effects to improve accuracy. It is then possible to extract quantitative data using a pixel averaging of multiple pixels of similar composition to obtain a more precise measurement, such as discussed previously. It is also possible to work on other statistical data such as histograms of composition to delineate for instance, the modal abundance of an anorthite-rich core versus an albitized domain (Fig. 4e).

It is also possible to calculate the detection limits and analytical sensitivity just as it is done for single point analyses (Fig. 5). At the analytical conditions considered here (50 nA, 50 ms per pixel), the per pixel calculated analytical sensitivity (~2-5% for major, >10-20% for minor element) and detection limit (typically between 0.06 and 0.15 wt% in this example) remains of course high, when compared to point analysis, but can be further improved through pixel aggregation or with longer counting time, higher beam current, or more optimal spectrometer selection (e.g., large area monochromator, P-10 vs. Xe counter). For cleanliness of the output, the analytical sensitivity calculations can be skipped for any pixel yielding a concentration <1 wt%, as it usually yields very high and meaningless values (gray pixels).

Comparing Raw Intensity Maps to Matrix Effect Corrected Maps

Traditionally, raw intensity WDS and EDS X-ray maps were used for the documentation and interpretation of chemical variation in solid materials. For several decades, EDS X-ray maps have been quantitative (at least when standards are utilized), because it was relatively easy to do so. While the importance of matrix corrections in WDS spot analyses is universally acknowledged, lack of computing power and software development has posed a hindrance in extending robust corrections to WDS X-ray maps. However, in situations that require significant absorption correction for X-ray intensities, substantial discrepancies can be observed between raw and quantified maps. Figure 6 is one example for such a case, showing a Fe-Ti oxide grain with Fe-rich core and exsolutions of ilmenite ($FeTiO_3$) and titanite ($CaTiSiO_5$).

The raw X-ray map of oxygen (Fig. 6a) would suggest relatively constant oxygen contents across the mineral grain, while the fully quantified map (Fig. 6b) shows pronounced differences in oxygen concentrations. Maps of net and background intensities (Fig. 6c,d) calculated by MAN show a slight increase in background intensities in the core but a negligible difference in net counts due to the high peak-to-background ratios for oxygen across all phases. Therefore, neither a background-corrected map by itself, nor a quantification using a calibration curve, would accurately reveal the varying oxygen contents.

In this example, emitted O Kα X-ray intensities in the Fe-Ti oxides are dominantly controlled by the changes in mass absorption of O Kα by Fe, Ti, or O itself. Mass absorption coefficients for O in Ti and Fe, respectively, differ by almost an order of magnitude (Ti: 22422 vs. Fe: 3625; FFAST database; Chantler, 2000; Chantler et al. 2005). Consequently, for a given oxygen wt% content, areas high in Fe will show higher relative O Kα intensities, whereas Ti-rich areas will

show lower X-ray intensities as they will be absorbed more. Only a full quantification, including a background and matrix correction (and interference correction), can adequately account for this change in X-ray emission rates. It is therefore essential that the analyst rigorously quantify each pixel using the methods described in this paper, so that they can be confident that differences in concentrations and zoning are not masked or introduced by variations in background intensities, absorption and fluorescence effects between grains or mineral domains.

Trace Element Quantification in X-ray Maps

Rigorous quantification is essential in order to facilitate accurate evaluation of X-ray intensity maps of elements with trace concentrations (>10 to 1000ppm). The crucial point for accurate trace analysis is the correction for the X-ray continuum contribution to the measured X-ray intensity at the Bragg conditions for the characteristic X-ray of interest (see Jercinovic et al., 2012; Allaz et al., 2019a), because continuum intensity varies as a function of the mean atomic number of a given phase, and also from absorption effects associated with the composition of the phase. An accurate EPMA trace element analysis, whether it is by single point analysis or by pixel mapping, can only be accomplished with an accurate and precise background correction. This means that the continuum must be accurately calculated or measured, for each pixel, with a precision sufficient to answer the analytical questions at hand.

Bremsstrahlung correction can be problematic for multi-phase element mapping, where each phase has a potentially different average atomic number. It can also be problematic for a single phase that displays a significant compositional zonation inducing a significant change in average Z-number (e.g., Z-bar ~10.7 to 11.9 between albite and anorthite). This issue gets even more

646 complicated when multiple substitutions are possible in a strongly heterogeneous phase, and
647 when both light and heavy elements are substituting (e.g., in zircon: Zr <=> [Hf, U, Th], Si+Zr
648 <=> P+REE, etc.).

649 As previously described, when acquiring EPMA trace element point measurements, typically the
650 background X-ray intensity is sampled by de-tuning each WDS spectrometer to both the high
651 and low sides of the characteristic X-ray peak, implying at least a doubling of the acquisition
652 times. Fortunately, we can also apply the MAN background correction to X-ray maps, just as it is
653 applied to point analyses. Once a MAN background calibration curve is defined for each element
654 to be mapped, there is no need to measure a background map.

655 Figure 7 compares the quantification of trace element maps of Hf Lα, Y Lα, P Kα, U Mα, and
656 Th Mα in zircon using off-peak map acquisitions (employing two WDS spectrometer positions
657 with a linear interpolation of the off-peak map pixel intensities), and also using the MAN
658 background correction, with both methods utilizing the same on-peak map intensities. The ZrO_2
659 and SiO_2 contents were constrained by assuming a mineral formula by difference from 100%.
660 This is accomplished by including the calculated $ZrSiO_4$ (by difference from the measured
661 elements) into the matrix correction during the matrix iteration calculations so that an accurate
662 matrix and average atomic number (for the MAN interpolation) is obtained. In addition, it should
663 be noted that a correction for the interference of Th Mβ on U Mα should normally be applied.
664 However, in this example, the Th content is barely above detection limit and therefore a spectral
665 interference correction is unnecessary in this particular case.

666 Somewhat unintuitively, the use of MAN background calibrations actually improves precision
667 because the background intensity calculation is no longer limited by continuum statistics, but is
668 instead based on our major element concentrations, which solely determine the average atomic

669 number of the matrix, and hence the precision (and accuracy) of the absorption-corrected MAN
670 background curve. Both background correction routines yield equally accurate results, yet the
671 MAN background corrected maps (Fig. 7a) yields more precise results with less noise (especially
672 visible on U and Th maps). These MAN background calibrations can result in accuracy errors for
673 trace elements on the order of a few hundred ppm in typical geological materials, though this can
674 be accurately compensated for by use of the "blank" correction (Donovan et al., 2011). However,
675 the pixel level measurement precision in our X-ray maps is limited by the pixel dwell time (and
676 beam current), and in most situations it is significantly worse than the accuracy obtained with the
677 MAN background correction.

678 Even with a cursory visual examination of the off-peak and MAN background corrected trace
679 elements maps, the MAN-corrected quantitative element maps clearly provide improved
680 precision/sensitivity compared to the off-peak background corrected maps, without the need of
681 doubling or tripling the acquisition time in order to obtain background maps. Another advantage
682 of the MAN correction is that is reduces the risk of acquiring a background map at a wavelength
683 (off-peak) position that could be interfered with by another major or minor element present only
684 in a few phases or in a specific zone of the area to be mapped.

685 The higher sensitivity seen in the MAN background corrected maps is due to the fact that when
686 the on-peak intensities are corrected for background, the variances of the on and off-peak
687 intensities are added in quadrature:

688 $$\sigma_{P-B} = \sqrt{\sigma_P^2 + \sigma_B^2} \quad \text{(Eq. 8)}$$

689 In practice, this means that as the measured concentration approaches zero, and therefore the
690 variances of the on-peak and off-peak become similar, the precision of the background intensity

becomes as important as the precision of the on-peak measurement. In a classical two-point background acquisition, the error on the two-background measurement is limited to only continuum counting statistics, which due to the relatively low intensity, results in a relatively low precision background correction. On the other hand, because the error on a MAN-calibrated background correction is limited primarily by the measurement precision of the major elements (e.g., the variance of the average atomic number of the material from the high concentration elements), the variance of the interpolated background intensity is much smaller (see Donovan et al., 2016 for a discussion of these statistical considerations). In fact, typically the resulting precision of the MAN net intensity background is approximately 40% better than traditional off-peak corrections (by the square root of two), because the background variance term in Eq. 8 (σ_B^2) approaches zero, particularly when the major matrix elements are specified by difference or fixed concentration). Therefore it is primarily only the precision of the on-peak measurement term (σ_P^2 in Eq. 8), which contributes to the net intensity precision, when the MAN background method is utilized.

Correction of Spectral Interferences in X-ray Maps

Correction of spectral interferences is also particularly critical for accurate quantitation of trace elements where a trace element X-ray emission line is overlapped by a significant emission line from another element. This problem is illustrated by obtaining X-ray maps for S Kα, Fe Kα, Cu Kα (Fig. 8a-c), and Mo Lα (Fig. 8d-f) from a sample containing the phases pyrite (FeS_2) and chalcopyrite ($CuFeS_2$). These maps are followed by the extraction of a cross-section A-B across the pyrite-chalcopyrite interface (Fig. 8g, h). The Mo contents of both sulfides are expected to be

713 at the trace level, most likely below the detection limit of the map measurement sensitivity. Yet,
714 the raw counts (Fig. 8d) apparently reveal the presence of significant Mo. This apparent Mo
715 signal mostly comes from the strong interference of Mo Lα by S Kα on a PET monochromator,
716 and therefore a correction for spectral interference is essential for Mo accuracy. Without a peak
717 interference correction (Fig. 8e), up to 1.8 and 1.2 wt% Mo is erroneously measured in pyrite and
718 chalcopyrite, respectively. When a quantitative interference correction is applied (Donovan et al.,
719 1993), data essentially yield values at or below detection limit (~700 ppm at the mapping
720 conditions utilized), as seen in Figure 8f.

721 Interestingly, visualization of the spatial distribution of an element that has a large compositional
722 range, can be also problematic. For example, the Cu element map in Figure 8c shows levels of
723 Cu approaching zero in pyrite (phase on left), but around 33 wt% in chalcopyrite (phase on
724 right). One solution to this visualization problem is the use of logarithmic weight percent values
725 to scale the element map. Figure 9 shows the application of a logarithmic scale to the Cu wt%
726 values and subsequently elucidates an apparent increase in Cu up to ~1 wt% in pixels adjacent to
727 the chalcopyrite boundary (Fig. 9b); an observation that otherwise might have been missed. In
728 this specific example, the apparent presence of Cu at the grain boundary is not related to
729 diffusion, but is rather an artifact from secondary fluorescence effect from the bremsstrahlung
730 (e.g., Borisova et al., 2018).

731

732 ***Quantification of Beam Sensitive Samples or TDI Scanning***

733 The electron beam can cause many materials to suffer from ion diffusion, recrystallization,
734 amorphization, or even volatilization (e.g., loss of OH, H_2O, or CO_2 groups) chiefly due to the

735 heat (phonon excitation) generated by incident electron interaction with matter (Hughes et al.,
736 2019). In such cases, where the beam current cannot be reduced or defocused, and a high thermal
737 conductivity coating (e.g., Al, Ag or Ir), is not appropriate, it is recommended to apply a time-
738 dependent intensity (TDI) correction that can account for the ion migration and/or a change in
739 signal due to physical changes in the analyzed material, provided it follows a linear, exponential,
740 or polynomial trend over time. These so-called beam sensitive materials can be extremely
741 difficult to analyze using single-point analysis due to the limited analytical time available before
742 the material is so badly damaged that even a TDI correction cannot account for the change (e.g.,
743 Allaz et al. 2019b).

744 Among the classic examples in the literature are, for instance, phosphates (e.g., Goloff et al.
745 2012; Fialin and Chopin, 2006), alkali-rich phases (e.g., Gedeon et al., 2008), and carbonates
746 (e.g., Zhang et al., 2019). One extreme example concerns hydrated alkali-sulfate (natro-) jarosite
747 and (natro-) alunite $(K,Na)(Al,Fe)_3(SO_4)_2(OH)_6$ displaying fine compositional variation at the
748 scale of ~1-5 μm. Irremediable Na or K diffusion and a concomitant increase or decrease in Fe,
749 Al, and S happens within less than 10 seconds of analyzing a single point at less than 2 nA with a
750 slightly defocused beam (2-3 μm). Beyond this, the beam damage induces a large change in the
751 major elements and a TDI correction must be applied. In this case, it is possible to run analyses
752 at 10 nA for 20 s using a focused electron beam, and to correct for the beam damage effects.
753 Beyond this point, the damage may become so severe that an accurate TDI correction cannot be
754 applied. Notwithstanding a total electron dose of only 200 nA·s, and with the use of the TDI
755 correction, the analytical precision is typically poor. Multiple point analyses in a homogeneous
756 domain are then required to obtain a good precision, which can be problematic when the material

757 to analyze is finely zoned at the micron-scale and in very small grains (typical grain-size in the
758 sample under investigation is ~20 μm; Potter-McIntyre and McCollom, 2018).

759 Another solution to obtain equally precise and sometimes better accuracy quantitative analyses
760 of such complexly zoned beam sensitive materials is to acquire element maps and apply a TDI
761 correction during the map quantification. To do this, a time series of beam (or stage) scanned
762 maps over an area are acquired with multiple (replicate) mapping frames. The TDI correction
763 can then be applied on each individual pixel using these multiple frames to extrapolate the pixel
764 intensity at time t = 0 s (beginning of the mapping elapsed time for each individual pixel). Figure
765 10 is an example of such TDI-corrected element maps of Na-free jarosite (see Potter-McIntyre
766 and McCollom, 2018 for detail on sample MN05, notably their Fig. 10). Multiple test maps for K
767 Kα, S Kα, Fe Kα, Al Kα and As Lα are run using either 50 or 100 nA beam currents, different
768 counting times (5, 10, 20, and 40 ms per pixel on one frame) and total number of frames (8
769 frames at 5 ms, 5 frames for all others), resulting in a variation of total beam dose of 2 to 20
770 nA·s. Due to the beam damage induced by each test, it is not possible to re-analyze the same
771 area. For the quantification of each map, the MAN background method is used, and the water-
772 content is recalculated by stoichiometry assuming 6 hydrogen atoms for a total of 14 oxygens
773 and included in the iterated matrix correction routine (Fig. 2). Results obtained with and without
774 the TDI correction are then compared, along with a comparison of data obtained on the first and
775 the last frame (labelled respectively “TDI”, “Aggregated”, “First”, and “Last” in Figure 10).

776 At low beam dose (total of 2 nA·s per pixel; Fig. 10a), both the TDI-corrected maps and the
777 aggregated maps yield identical results within their respective errors. It is clear from visual
778 inspection and counting statistics that the TDI results are slightly less precise due to the nature of
779 the TDI correction extrapolation. At intermediate to high beam doses (e.g., 4 and 10 nA·s; Fig.

10b,c), the results of the aggregated maps degrade: zones are getting enriched or depleted in K_2O, and in parallel SO_3 and Fe_2O_3 either decrease or increase at high beam dose, and overall the analytical totals increase. This can be clearly seen numerically in the averaged-pixel quantitative data (Fig. 10d), especially when comparing the data from the first and the last maps. It is also interesting to notice that there is no systematic diffusional loss of K, rather there are "sink and hole" areas where K diffuses in or out. This effect is illustrated in Figure 11 with a map of the TDI correction percentage for the measurement of K Kα, S Kα , and Fe Kα over five passes at 100 nA and 20 ms per pixel (see also Fig. 10c).

Trace Elements and Spectrometer Aggregation

Quantification of multiple phase X-ray maps can be easily done with great precision and accuracy for major and minor element analyses, but the counting statistics usually prohibits mapping for trace elements without excessively long acquisition times at high currents. If a high current is not applicable (e.g., beam sensitive materials) or if the analyst aims at reducing the total acquisition time, it is recommended to use multiple WDS detectors in parallel to analyze a single element. Figure 12 presents an X-ray map of a multiphase area in a rhyolite sample composed of glass, plagioclase, and K-feldspar. Previous single-point analyses and observations in BSE images suggest a strong Ba-enrichment at the rim of K-feldspar. Maps were acquired in two passes, with a first pass for the major elements (Si Kα, Al Kα, Ca Kα, Na Kα, and K Kα), and a second mapping pass with only Ba Lα analysis on three PET-L spectrometers. Of the major elements expected in this sample, only Fe was not mapped, as it is a trace concentration in these specific feldspars, and only present at level around 2.5 wt% in the glass. All other elements

(Mg, Ti, Sr, etc.) are below 1000 ppm. The presence of Ti could potentially be a problem for Ba analysis due to the mutual interference of Ti Kα on Ba Lα. However, single-point analyses including a correction for this mutual Ti Kα <=> Ba Lα interference yield low Ti-content: <3000 ppm in glass and <500 ppm in feldspar minerals. At this level, a correction for Ti interference on Ba is minimal and below the sensitivity of Ba Lα element map (calculated Ba detection limit of ~500 ppm). These duplicate element maps allows one to not only highlight and quantify the high-Ba content in K-feldspar, but also to accurately and precisely analyze Ba even in the glass (~1200 ppm). These element maps were essential for the data interpretation, as only the maps clearly reveal a two-step growth. The primary feldspar, which is richer in albite (Na)-component, suffered a partial resorption (e.g., irregular internal zonation in K and Ca, top-right corner of Fig. 12c), and the Ba-rich K-feldspar rim and the anorthite(Ca)-richer plagioclase rim both represent a second magmatic event.

Implications

Rigorous quantification of X-ray maps is critically important for accurate interpretation of element distributions, not only for minor and trace elements, but also elements whose emission lines suffer significant absorption or fluorescence. Raw X-ray maps remain an essential tool to reveal two-dimensional variation that cannot be fully ascertained by discrete point analysis. However, because the same raw X-ray line intensity can represent quite different concentrations in different phases, due most notably to significant differences in X-ray absorption effect, but also from changes in background intensities (and potential issues stemming from spectral interferences), without quantification at the pixel level it would be significantly more risky to

draw robust conclusions from merely qualitative X-ray maps. Moreover, this rigorous quantification protocol ensures that all maps can be compared one-to-one, even if they were acquired at different times, using different spectrometers, in different laboratories, or at different analytical conditions, etc.

Applications of element map analysis by EPMA (WDS or EDS) are numerous, and the ability to quantify them with accuracy and precision makes these applications even more attractive to researchers. Firstly, geological materials are often the product of a complex mineral growth, partial dissolution (resorption), and reprecipitation history, the interpretation of which is critical to developing an understanding of large-scale geological processes. Up until now, element maps were often only used for qualitative observations (e.g., identifying inherited core, retrogression, diffusion profile, etc., which subsequently required quantification by careful single-point analysis) or for approximate quantification (e.g., using a two-point calibration method in a single compositionally zoned phase). However, with the level of accuracy and precision achieved with the proposed map quantification methodology, the qualitative map data becomes quantitative data, with an accuracy comparable to a single point analysis, and with an equally good precision when pixel averaging is considered. Secondly, material scientists can now observe accurately and with high sensitivity, diffusion profiles, identify and quantify exsolutions, or perform homogeneity tests. Additionally, the "analytical totals" map can also uncover previously unrecognized secondary fluorescence, i.e., pixels where the totals are consistently > 100% (Fournelle at al., 2005). By extension, a more accurate "local" composition can be obtained in finely grained material (e.g., partially re-crystallized glass or quenched material, exsolutions lamellae, etc.), without the need to acquire multiple discrete points on which the resulting accuracy can be questionable, due to the inhomogeneous nature of the analyzed material.

847 Finally, the complementary use of the MAN background correction method allows one to apply
848 an accurate background correction, without the need to physically acquire additional background
849 intensity maps with a resulting doubling (at least) of the total acquisition time. The use of
850 spectral interference correction and TDI correction routines also ensure that no such artifacts are
851 present in the quantitative maps. As it follows the rigor and protocols of single point analysis,
852 this proposed mapping quantification method is most likely the best we can do, at present, in
853 terms of accuracy for WDS X-ray map quantification. The acquisition of quantitative X-ray
854 maps affords the analyst valuable quantitative data in less time, when compared to a series of
855 discrete point analysis in compositionally zoned materials or strongly heterogeneous materials,
856 or when the material is extremely beam sensitive.

857

858 # Acknowledgements

859 The authors wish to thank all those who over the years who have contributed to the effort to
860 quantify WDS X-ray maps from EPMA instruments. A partial list would include Brian Gaynor,
861 Aoife McFadden, Michael Matthews, Gareth Hatton, Benjamin Wade, Jon Wade, Karen Wright,
862 Ben Buse, Stuart Kearns, Daniel Ruscitto, Malcolm Roberts, David Adams, David Wark, Philipp
863 Poeml, Philippe Pinard, John Fournelle, and Michael Jercinovic. The latter two are also thanked
864 for their most helpful and quite detailed reviews of the manuscript. We thank Alina Fiedrich for
865 providing the Adamello tonalite sample (Figs. 4, 5), Tom McCollom for the jarosite sample
866 (Figs. 10, 11), and Matthew Brueseke and Ben Ellis for the rhyolite sample (Fig. 12). All
867 electron microprobe works presented here were acquired on one of the following instruments:
868 Cameca SX-100 at the CAMCOR center (Oregon University, NSF EAR-0345908 and the

869 Murdoch Foundation), JEOL-8230 at the University of Colorado Boulder (NSF EAR-1427626),
870 JEOL-8530F at the University of Minnesota Minneapolis (NSF EAR-1625422), and JEOL-8230
871 at ETH Zürich. The authors are thankful to their respective National Science agencies and
872 universities that made possible the purchase of these instruments.

873

874 References

875 Allaz, J.M., Williams, M., Jercinovic, M., Goemann, K., and Donovan, J. (2019a) Multipoint
876 Background Analysis: Gaining Precision and Accuracy in Microprobe Trace Element
877 Analysis. Microscopy and Microanalysis, 25(1), 30-46.

878 Allaz, J.M., Popa, R.G., Reusser, E., and Martin, L. (2019b) Electron Microprobe Analysis of
879 Minor and Trace Elements in Beam Sensitive Materials: How Far Can We Go? Microscopy
880 and Microanalysis, 25(S2), 2312-2313.

881 Armstrong, J.T. (1988) Quantitative Analysis of Silicate and Oxide Materials: Comparison of
882 Monte Carlo, ZAF, and Procedures. Microbeam Analysis, 239-246.

883 Barkman, J., Carpenter, P., Zhao, J., and Donovan, J. (2013). Electron Microprobe Quantitative
884 Mapping vs. Defocused Beam Analysis. Microscopy and Microanalysis, 19(S2), 848-849.

885 Bastin, G.F., and Heijligers, H.J.M (1991) Quantitative electron probe microanalysis of ultra-
886 light elements (boron - oxygen). In K.F.J. Heinrich and D.E. Newbury, Eds., Electron Probe
887 Quantitation, p. 145-161. Plenum Press, NY.

888 Batanova, V.G., Sobolev, A.V., and Kuzmin, D. V. (2015). Trace element analysis of olivine:
889 High precision analytical method for JEOL JXA-8230 electron probe microanalyser.
890 Chemical Geology, 419, 149-157.

891 Borisova, A.Y., Zagrtdenov, N.R., Toplis, M.J., Donovan, J.J., Llovet, X., Asimow, P.D., de
892 Parseval, P., and Gouy, G. (2018) Secondary fluorescence effects in microbeam analysis
893 and their impacts on geospeedometry and geothermometry. Chemical Geology, 490, 22-29.

894 Carpenter, P.K., Zeigler, R.A., Jolliff, B.L., Vicenzi, E.P., Davis, J.M., and Donovan, J.J. (2009)
895 Advances in electron-probe microanalysis and compositional mapping: Applications to
896 lunar samples. 40th Lunar and Planetary Science Conference, The Woodlands, TX, 2531.

897 Carpenter, P.K., and Hahn, T. (2017) New Developments in Compositional Stage Mapping by
898 EPMA and Micro-XRF. Microscopy and Microanalysis, 23(S1), 1068-1069.

899 Chantler, C.T. (2000) Detailed Tabulation of Atomic Form Factors, Photoelectric Absorption
900 and Scattering Cross Section, and Mass Attenuation Coefficients in the Vicinity of
901 Absorption Edges in the Soft X-Ray (Z=30-36, Z=60-89, E=0.1 keV-10 keV), Addressing
902 Convergence Issues of Earlier Work. Journal of Physical and Chemical Reference Data, 29,
903 597-1048.

904 Chantler, C.T., Olsen, K., Dragoset, R.A., Chang, J., Kishore, A.R., Kotochigova, S.A., and
905 Zucker, D.S. (2005) X-Ray Form Factor, Attenuation and Scattering Tables (version 2.1).
906 [Online] Available: http://physics.nist.gov/ffast [2020, July 29]. National Institute of
907 Standards and Technology, Gaithersburg, MD.

908 Crisci, F., Durand-Charre, A., and Jouanne, D. (2006) Practical Aspects of Carbon Content
909 Determination in Carburized Steels by EPMA. Microscopy and Microanalysis, 12(4), 331-
910 334.

911 Donovan, J.J., Snyder, D.A., and Rivers, M.L. (1993) An improved interference correction for
912 trace element analysis. Microbeam Analysis, 2, 23-28.

913 Donovan, J.J., and Tingle, T.N. (1996) An Improved Mean Atomic Number Correction for
914 Quantitative Microanalysis. Journal of Microscopy and Microanalysis, 2, 1-7.

915 Donovan, J.J., Lowers, H.A., and Rusk, B.G. (2011) Improved electron probe microanalysis of
916 trace elements in quartz. American Mineralogist, 96(2-3), 274-282.

917 Donovan, J.J., Singer, J.W., and Armstrong, J.T. (2016) A new EPMA method for fast trace
918 element analysis in simple matrices. American Mineralogist, 101(8), 1839-1853.

919 Donovan, J., Pinard, P., and Demers, H. (2019) High Speed Matrix Corrections for Quantitative
920 X-ray Microanalysis Based on Monte Carlo Simulated K-Ratio Intensities. Microscopy and
921 Microanalysis, 25(3), 735-742.

922 Eichen, E., Tabock, J., and Kinsman, K.R. (1972) An electron-microprobe technique for
923 detecting low carbon concentrations in iron. Metallography, 5(2), 151-162.

924 Fialin, M., and Chopin, C. (2006) Electron-beam (5-10 keV) damage in triplite-group
925 phosphates: Consequences for electron-microprobe analysis of fluorine. American
926 Mineralogist, 91(4), 503-510.

927 Fiedrich, A.M., Bachmann, O., Ulmer, P., Deering, C.D., Kunze, K., and Leuthold, J. (2017)
928 Mineralogical, geochemical, and textural indicators of crystal accumulation in the Adamello
929 Batholith (Northern Italy). American Mineralogist, 102(12), 2467-2483.

930 Fournelle, J. H., Kim, S., & Perepezko, J. H. (2005). Monte Carlo simulation of Nb Kα
931 secondary fluorescence in EPMA: comparison of PENELOPE simulations with
932 experimental results. *Surface and Interface Analysis: An International Journal devoted to*
933 *the development and application of techniques for the analysis of surfaces, interfaces and*
934 *thin films*, *37*(11), 1012-1016.

935 Gedeon, O., Zemek, J., and Jurek, K. (2008) Changes in alkali-silicate glasses induced with
936 electron irradiation. Journal of Non-Crystalline Solids, 354(12-13), 1169-1171.

937 Goldstein, J.I., Newbury, D.E., Echlin, P., Joy, D.C., Firori, C., and Lifshin E. (1992) Scanning
938 Electron Microscopy and X-ray Microanalysis, 550 p., Springer-Verlag, New York (USA).

939 Goloff, B., Webster, J.D., and Harlov, D.E. (2012). Characterization of fluor-chlorapatites by
940 electron probe microanalysis with a focus on time-dependent intensity variation of
941 halogens. American Mineralogist, 97, 1103-1115.

942 Hughes, E.C., Buse, B., Kearns, S.L., Blundy, J.D., Kilgour, G., & Mader, H.M. (2019). Low
943 analytical totals in EPMA of hydrous silicate glass due to sub-surface charging: Obtaining
944 accurate volatiles by difference. *Chemical Geology*, *505*, 48-56.

945 Jercinovic, M.J., Williams, M.L., Allaz, J., and Donovan, J.J. (2012). Trace analysis in EPMA.
946 IOP Conference Series: Materials Science and Engineering, 32, 1-22.

947 Kramers, H.A. (1923) On the theory of X-ray absorption and of the continuous X-ray spectrum.
948 Phil Mag, 46, p. 836

949 Lanari, P., Vidal, O., De Andrade, V., Dubacq, B., Lewin, E., Grosch, E.G., and Schwartz, S.
950 (2014) XMapTools: A MATLAB©-based program for electron microprobe X-ray image
951 processing and geothermobarometry. Computers and Geosciences, 62, 227-240.

952 Merlet, Claude, and Jean-Louis Bodinier. "Electron microprobe determination of minor and trace
953 transition elements in silicate minerals: A method and its application to mineral zoning in
954 the peridotite nodule PHN 1611." *Chemical Geology* 83.1-2 (1990): 55-69.

955 Morgan, G.B. and London, D., 1996. Optimizing the electron microprobe analysis of hydrous
956 alkali aluminosilicate glasses. *American Mineralogist*, *81*(9-10), pp.1176-1185.

957 Moy, Aurélien, John H. Fournelle, and Anette Von Der Handt. "Solving the iron quantification
958 problem in low-kV EPMA: An essential step toward improved analytical spatial resolution
959 in electron probe microanalysis—Olivines." *American Mineralogist: Journal of Earth and*
960 *Planetary Materials* 104.8 (2019): 1131-1142.

961 Newbury, D.E. (1995) Artifacts in Energy Dispersive X-Ray Spectrometry in Electron Beam
962 Instruments. Are Things Getting Any Better?. In D.B. Williams, J.I. Goldstein, D.E.
963 Newbury, Eds., X-Ray Spectrometry in Electron Beam Instruments, p. 167-201. Springer,
964 Boston, MA.

965 Newbury, D., and Ritchie, N. (2019) Electron-Excited X-ray Microanalysis by Energy
966 Dispersive Spectrometry at 50: Analytical Accuracy, Precision, Trace Sensitivity, and
967 Quantitative Compositional Mapping. Microscopy and Microanalysis, 25(5), 1075-1105.

968 Nielsen, C.H., and Sigurdsson, H. (1981) Quantitative methods for electron microprobe analysis
969 of sodium in natural and synthetic glasses. American Mineralogist, 66, 547-552.

970 Ortolano, G., Visalli, R., Godard, G., and Cirrincione, R. (2018) Quantitative X-ray Map
971 Analyser (Q-XRMA): A new GIS-based statistical approach to Mineral Image Analysis.
972 Computers and Geosciences, 115, 56-65.

973 Potter-McIntyre, S.L., and McCollom, T.M. (2018) Jarosite and alunite in ancient terrestrial
974 sedimentary rocks: Reinterpreting Martian depositional and diagenetic environmental
975 conditions. Life, 8, 32.

976 Tinkham, D.K., and Ghent, E.D. (2005) XRMapAnal: A program for analysis of quantitative X-
977 ray maps. American Mineralogist 90, 737 - 744.

978 Warren, P.H. (1997) The Unequal Host-Phase Density Effect in Electron Probe Defocused Beam
979 Analysis: an Easily Correctable Problem. 28th Annual Lunar and Planetary Science
980 Conference, Houston, TX, 1497-1498.

981 Zhang, X., Yang, S., Zhao, H., Jiang, S., Zhang, R., and Xie, J. (2019) Effect of Beam Current
982 and Diameter on Electron Probe Microanalysis of Carbonate Minerals. Journal of Earth
983 Science, 30(4), 834-842.

984

Table Captions

Table 1. Differences in Si concentrations from standard reference published values, where the concentrations are derived from an exponential fit calibration-curve method to the raw X-ray intensities, for synthetic zircon ($ZrSiO_4$) and synthetic forsterite (Mg_2SiO_4).

Table 2. Comparison of the average of all map pixels with published reference values for NBS K-411 mineral composition glass from NIST. The standards were MgO synthetic for Mg Kα, SiO_2 synthetic for Si Kα, and NBS K-412 mineral composition glass for Fe Kα, Al Kα, Ca Kα. n.a. = not analyzed.

Table 3. Evaluation of accuracy and precision for NIST standard K-411 by averaging various numbers of pixels from the quantitative X-ray maps compared to the average of 4 point analyses. Values for pixel variance (standard deviation) are consistent, while the standard error (around the average) decreases, with increasing pixel count as expected. n.a. = not analyzed.

Figure Captions

Figure 1. Example of an exponential calibration curve of Si concentrations as a function of X-ray intensities, for a number of standards each containing Si. Each green dot represents the average intensity for each standard. Errors on each standard measurement are smaller than the actual dot size (~0.5% relative for Si Kα intensity).

Figure 2. Flow chart of the proposed method for rigorously quantifying a series of raw intensity X-ray maps. These steps include normalization for pixel integration time, detector dead time, beam drift and standard drift (and optional off-peak map background corrections, TDI corrections and duplicate element aggregations), followed by iterative corrections for (MAN) background, matrix and spectral interferences on each pixel individually.

Figure 3. Quantified elemental X-ray maps for Si Kα, Fe Kα, Ca Kα, Al Kα and Mg Kα for the NIST K-411 silicate glass reference material, with a total weight-% map and an oxygen map calculated by stoichiometry with an additional 1.12% O to account for the presence of ferric iron, shown along with quantitative histograms and measured average and 3 standard deviation bar and certified values for each element (in red). Conditions were 15 keV, 30 nA, and 500 ms per pixel. Field of view is 63.5 x 63.5 μm. Note the analytical total map which is important just as it is for point analysis. These simple maps demonstrate that mapped pixels can achieve accuracy similar to normal point analyses, even though single pixel precision can be problematic without pixel averaging as seen in the map color scale ranges. See table 3 for a numerical summary.

1023 **Figure 4. (a)** Quantitative maps in oxide concentrations (wt%) for a feldspar grain from the
1024 Adamello tonalite; Kα lines were analyzed for all elements. Oxygen calculated by stoichiometry
1025 (not shown here). Conditions were 15 keV, 50 nA, and 50 ms per pixel. Field of view is 1.11 x
1026 1.644 mm at 3 μm/pixel resolution. **(b)** Formula basis maps for a feldspar grain based on 8
1027 oxygen atoms (apfu = atoms per formula unit). **(c)** Recalculated mineral end-member maps:
1028 albite (Na), anorthite (Ca), and K-feldspar (K). **(d)** Pixel filtering based on compositional limits
1029 and analytical totals. **(e)** Quantitative histograms of the previous pixel filtered quantitative maps.

1030

1031 **Figure 5.** Maps of the **(a)** relative analytical sensitivity (1σ), and **(b)** detection limit at 99%
1032 confidence (3σ) for Si, Al, Ca, Na, and K calculated for each individual pixel for a feldspar grain
1033 from the Adamello tonalite.

1034

1035 **Figure 6.** Element maps of a Fe-Ti mineral from the mafic-ultramafic Viravira Complex,
1036 Colombia. Conditions were 8 keV, 35 nA, and 100 ms per pixel. Oxygen Kα measured on LDE1
1037 monochromator, and PROZA91 matrix correction was applied with MAC values from FFAST
1038 database. Field of view is 414 x 274 μm. **(a,b)** The raw intensity X-ray map of O Kα **(a)** in the
1039 Fe-Ti-oxide mixture shows significant differences when compared to the fully quantified X-ray
1040 map **(b)**. **(c,d)** While the map of the calculated background intensities **(d)** correlates with Fe-rich
1041 core areas, the net intensities **(c)** are not affected due to the high peak-to-background ratios.

1042

1043 **Figure 7.** Quantitative X-ray maps of trace elements in a zircon grain using off-peak maps for
1044 the interpolated off-peak background map correction **(a)**, and alternatively using MAN

1045 background corrections (with the same on-peak map intensities) in **(b)**. Conditions were 15 keV,
1046 100 nA, and 1800 milliseconds per pixel (on-peak and total off-peak). Field of view is 38.1 x
1047 38.1 μm. Three separate map scans were acquired: the on-peak intensity maps, followed by the
1048 high off-peak intensity maps, followed by the low off-peak intensity maps. A comparison of the
1049 off-peak and MAN maps are seen in the cross sections for each element **(c)**. Note the
1050 improvement in precision particularly for U and Th cross sections with the MAN corrected maps
1051 (red lines) compared to the off-peak corrected X-ray maps (blue lines).

1052

1053 **Figure 8. (a-c)** Quantitative element maps of Fe, S and Cu. Conditions were 15 keV, 100 nA,
1054 and 1000 ms per pixel. Field of view is 127 x 127 μm. **(d)** Raw X-ray map of Mo Lα expressed
1055 as counts per second, **(e)** quantified X-ray map without a spectral interference correction, and **(f)**
1056 with interference correction. **(g,h)** Cross section A-B across the pyrite-chalcopyrite interface
1057 with and without a spectral interference correction. **(g)** Major element values are within the range
1058 of expected values for pyrite and chalcopyrite. Totals are very close to 100% in pyrite, and
1059 slightly lower in chalcopyrite most likely due to the presence of minor elements not analyzed. **(h)**
1060 Comparison of the Mo content with (Mo) or without (Mo*) the peak interference correction.
1061 Numerical data on the right side are average of concentration measurements along the profile
1062 (see "Quant 1" and "Quant 2" aside the profile). Error (1σ) indicated in parentheses.

1063

1064 **Figure 9.** Comparison of Cu element wt% map shown with **(a)** a linear or **(b)** a logarithmic
1065 scale. Using the logarithmic scale, the spurious low concentrations of Cu in pyrite due to
1066 secondary fluorescence across the phase boundary can be made visible, while avoiding

oversaturation of pixels with higher Cu content in chalcopyrite. **(c)** Plot of Cu wt% in pyrite versus the distance to the boundary with chalcopyrite.

Figure 10. Quantified X-ray maps of jarosite in sample MN05 using a beam map at 15 keV with a focused beam. Field of view is 50 x 50 μm at ~0.39 μm/pixel resolution. Three separate examples are shown with increasing electron beam dose: **(a)** 50 nA, 5 ms dwell time, 8 frames (= 2 nA·s), **(b)** 100 nA, 5 ms dwell time, 8 frames (= 4 nA·s), and **(c)** 100 nA, 40 ms dwell time, 5 frames (= 20 nA·s). For each test, the data was processed using either the TDI correction on each pixel, or by aggregating all intensities received on each frame (i.e., no correction for beam damage). All pixels yielding a low total below 80% were set to black in Figure 10. The table below lists the average of 100 pixels (area indicated on the SO_3 map) for the TDI corrected and aggregated data, respectively, along with the quantitative result considering only the first or the last acquired beam map frame. See text for discussion.

Figure 11. TDI correction (in relative percent) map for the analysis of K Kα, S Kα, and Fe Kα at 100 nA, 40 ms per pixel, and with 5 passes (total beam dose is 20 nA·s).

Figure 12. Quantitative element mapping in rhyolite, with focus on Ba-content in plagioclase, K-feldspar, and glass. Conditions were 15 keV, 100 nA, and 40 ms per pixel, 2 passes. Field of view is 329.5 x 229.5 μm at 0.5 μm/pixel resolution. **(a-f)** Quantitative map of SiO_2, Al_2O_3, CaO, Na_2O, K_2O, and total wt%. **(g)** Quantitative BaO wt% map obtained by aggregating the intensity of three spectrometers equipped with L-type (large) PET monochromators. **(h)**

Quantitative cross-section extracted from the map, as shown in **(g)**. Horizontal black lines over the BaO cross-section are precise data obtained from single-point quantitative analysis (longer counting time). **(i)** Quantitative single-point analysis shown for comparison; position of each analysis indicated in **(g)**.

Table 1

Si Kα, TAP, 20 keV, 30 nA	**$ZrSiO_4$**	**Mg_2SiO_4**
Published Concentration of Standard	15.32 wt%	19.96 wt%
Concentration from Calibration Curve (Fig. 1)	19.09 wt%	17.38 wt%
Relative error %	24.6%	-12.9%

Table 2

	Si wt%	Fe wt%	Mg wt%	Al wt%	Ca wt%	O wt%	Calc. O	Total
Average	25.06	11.18	8.63	0.02	10.98	1.12	42.93	**98.80**
Published	25.38	11.21	8.85	n.a.	11.06	1.12	43.56	**99.98**
Std Dev	0.72	0.64	0.15	0.02	0.20	0.00	0.86	**1.84**
Rel %	2.89	5.74	1.75	99.23	1.85	0.00	2.01	**1.86**
Minimum	22.28	8.43	8.06	-0.05	10.16	0.00	39.56	**91.77**
Maximum	27.84	14.17	9.25	0.13	11.82	0.00	46.38	**106.08**

Table 3

	Si wt%	Al wt%	Fe wt%	Mg wt%	Ca wt%	Integration time
NIST K-411 (Published)	25.38	n.a.	11.21	8.85	11.06	
NIST K-411 (Measured)	25.277	0.019	11.098	8.811	11.037	80 sec
4 Points Variance	0.037	0.004	0.082	0.027	0.025	
4 Points Error	0.019	0.002	0.041	0.014	0.013	
4 pixels Average	25.261	0.021	10.893	8.741	11.289	0.4 sec
4 pixels Variance	0.582	0.050	0.409	0.528	0.510	
4 pixels Error	0.291	0.025	0.205	0.264	0.255	
16 pixels Average	25.432	0.000	10.996	8.947	11.112	1.6 sec
16 pixels Variance	0.507	0.038	1.293	0.584	0.500	
16 pixels Error	0.127	0.010	0.323	0.137	0.125	
32 pixels Average	25.399	0.011	11.131	8.747	11.049	3.6 sec
32 pixels Variance	0.454	0.046	1.444	0.589	0.406	
32 pixels Error	0.076	0.008	0.241	0.098	0.068	
64 pixels Average	25.463	0.016	11.310	8.809	11.046	6.4 sec
64 pixels Variance	0.529	0.044	1.563	0.670	0.414	
64 pixels Error	0.066	0.001	0.195	0.084	0.052	
All pixels Average	25.353	0.016	11.057	8.748	10.994	1638 sec
All pixels Variance	0.494	0.048	1.427	0.593	0.460	
All pixels Error	0.004	0.001	0.011	0.005	0.004	

Figure 1

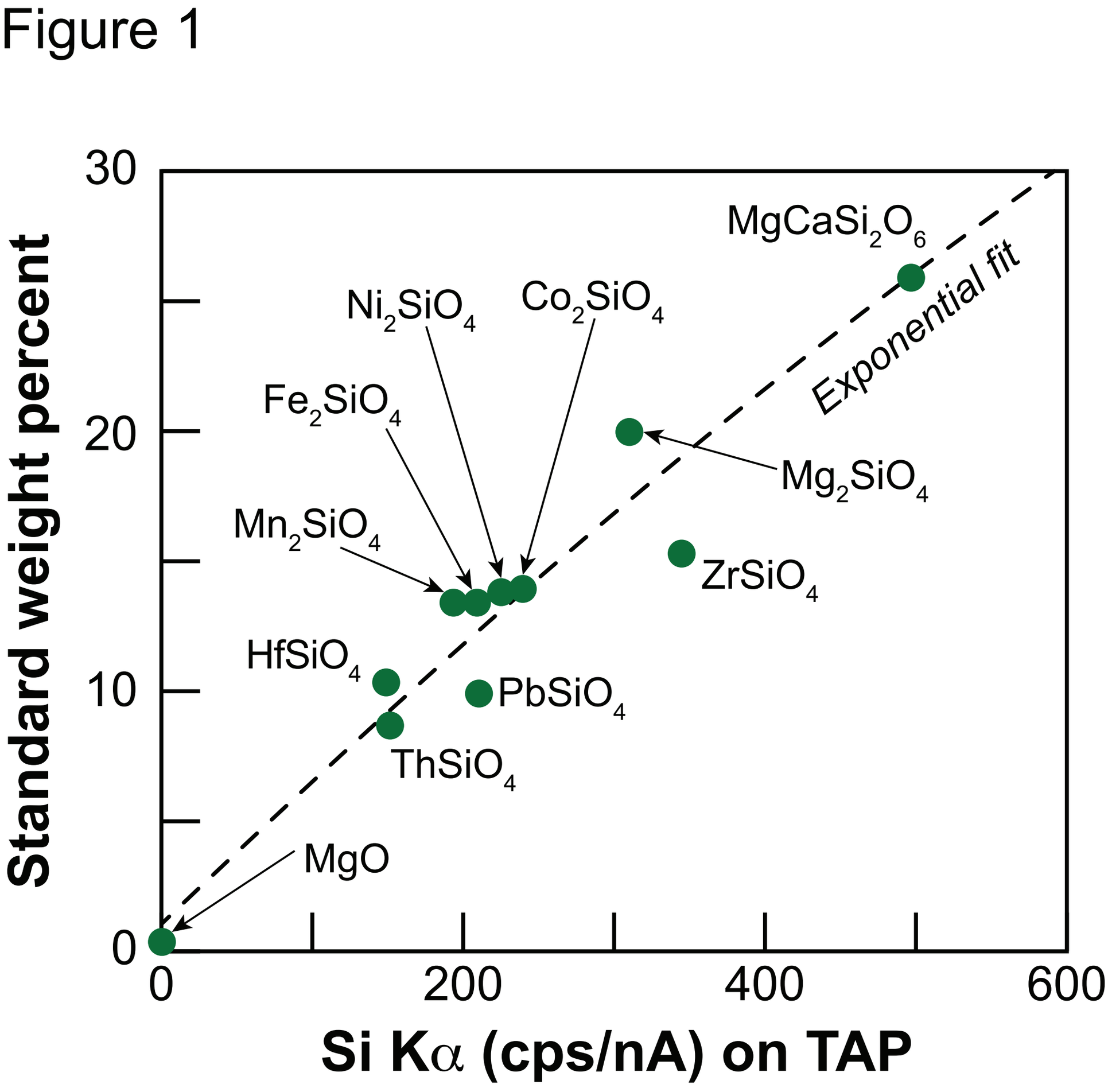
30
20
10
0
0
200
400
600
Standard weight percent
Si Kα (cps/nA) on TAP
MgCaSi2O6
Exponential fit
Ni2SiO4
Co2SiO4
Fe2SiO4
Mg2SiO4
Mn2SiO4
ZrSiO4
HfSiO4
PbSiO4
ThSiO4
MgO

Figure 2

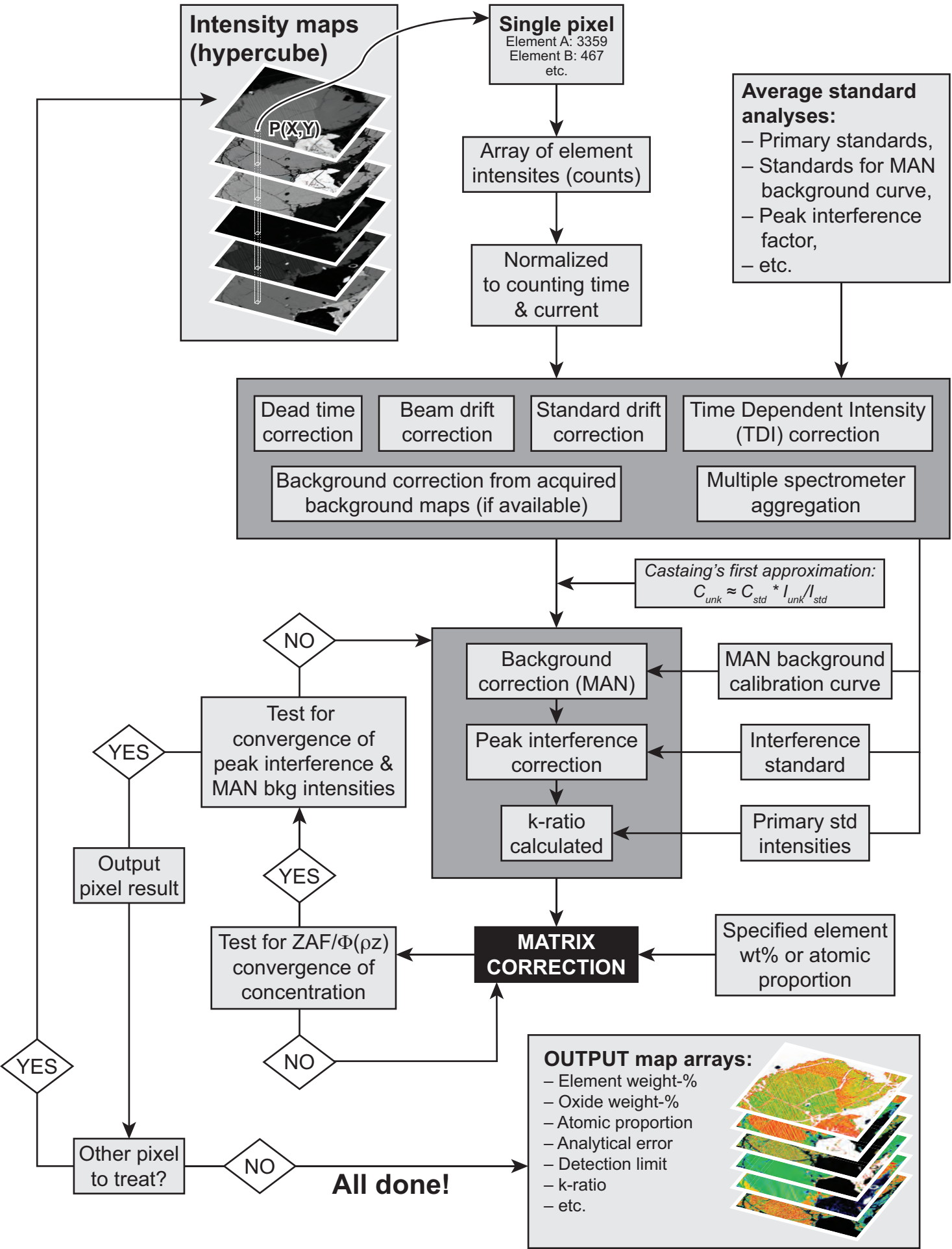
Intensity maps (hypercube)
P(X,Y)
Single pixel
Element A: 3359
Element B: 467
etc.
Array of element intensites (counts)
Normalized to counting time & current
Average standard analyses:
– Primary standards,
– Standards for MAN background curve,
– Peak interference factor,
– etc.
Dead time correction
Beam drift correction
Standard drift correction
Time Dependent Intensity (TDI) correction
Background correction from acquired background maps (if available)
Multiple spectrometer aggregation
Castaing's first approximation:
$C_{unk} \approx C_{std} * I_{unk}/I_{std}$
NO
Background correction (MAN)
MAN background calibration curve
Peak interference correction
Interference standard
k-ratio calculated
Primary std intensities
Test for convergence of peak interference & MAN bkg intensities
YES
Output pixel result
YES
Test for ZAF/Φ(ρz) convergence of concentration
MATRIX CORRECTION
Specified element wt% or atomic proportion
NO
YES
Other pixel to treat?
NO
All done!
OUTPUT map arrays:
– Element weight-%
– Oxide weight-%
– Atomic proportion
– Analytical error
– Detection limit
– k-ratio
– etc.

Figure 3

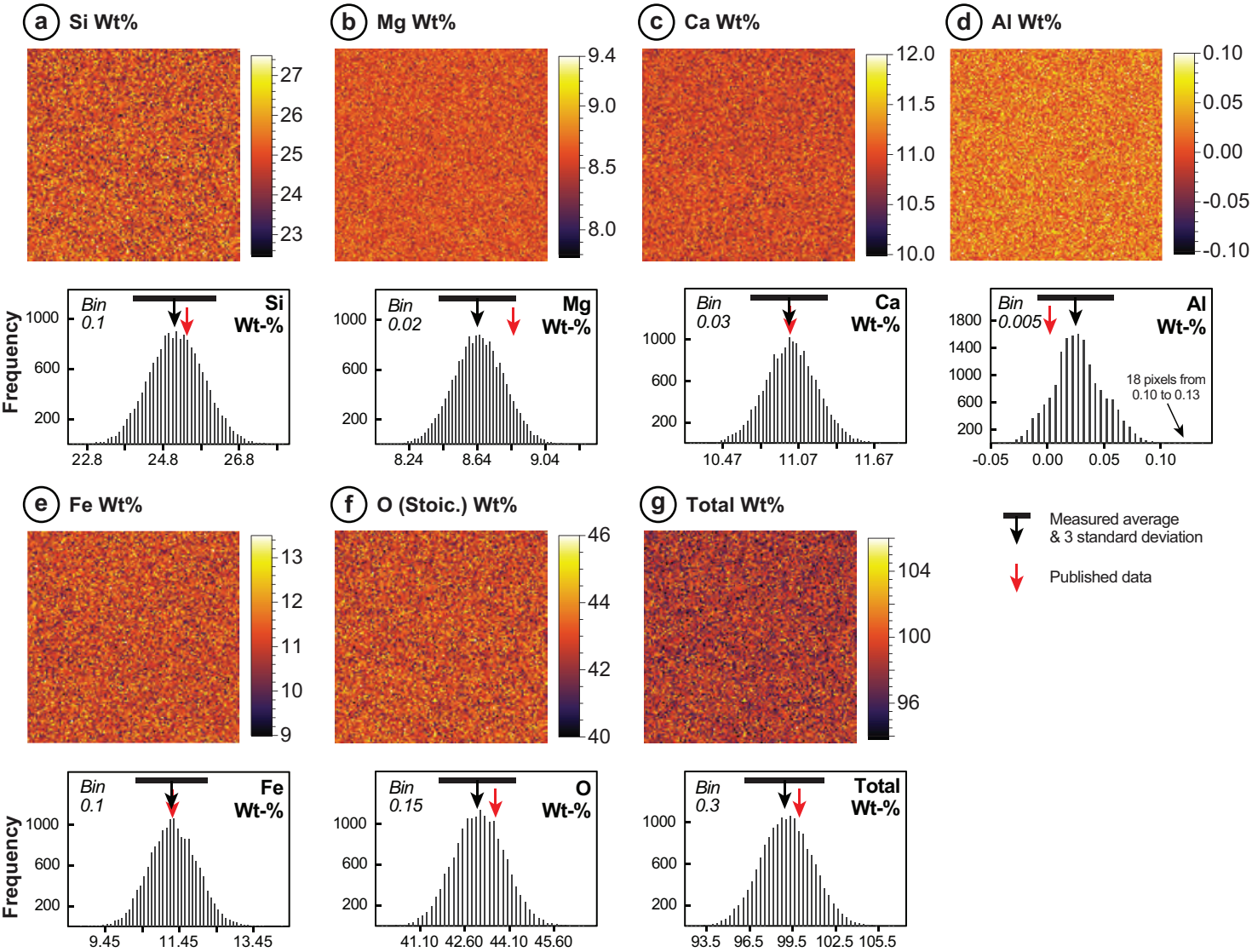
a Si Wt%
27
26
25
24
23
b Mg Wt%
9.4
9.0
8.5
8.0
c Ca Wt%
12.0
11.5
11.0
10.5
10.0
d Al Wt%
0.10
0.05
0.00
-0.05
-0.10
Frequency
Bin 0.1
Si Wt-%
1000
600
200
22.8
24.8
26.8
Bin 0.02
Mg Wt-%
8.24
8.64
9.04
Bin 0.03
Ca Wt-%
10.47
11.07
11.67
Bin 0.005
Al Wt-%
1800
1400
1000
600
200
-0.05
0.00
0.05
0.10
18 pixels from 0.10 to 0.13
e Fe Wt%
13
12
11
10
9
f O (Stoic.) Wt%
46
44
42
40
g Total Wt%
104
100
96
Bin 0.1
Fe Wt-%
9.45
11.45
13.45
Bin 0.15
O Wt-%
41.10
42.60
44.10
45.60
Bin 0.3
Total Wt-%
93.5
96.5
99.5
102.5
105.5
Measured average & 3 standard deviation
Published data

Figure 4

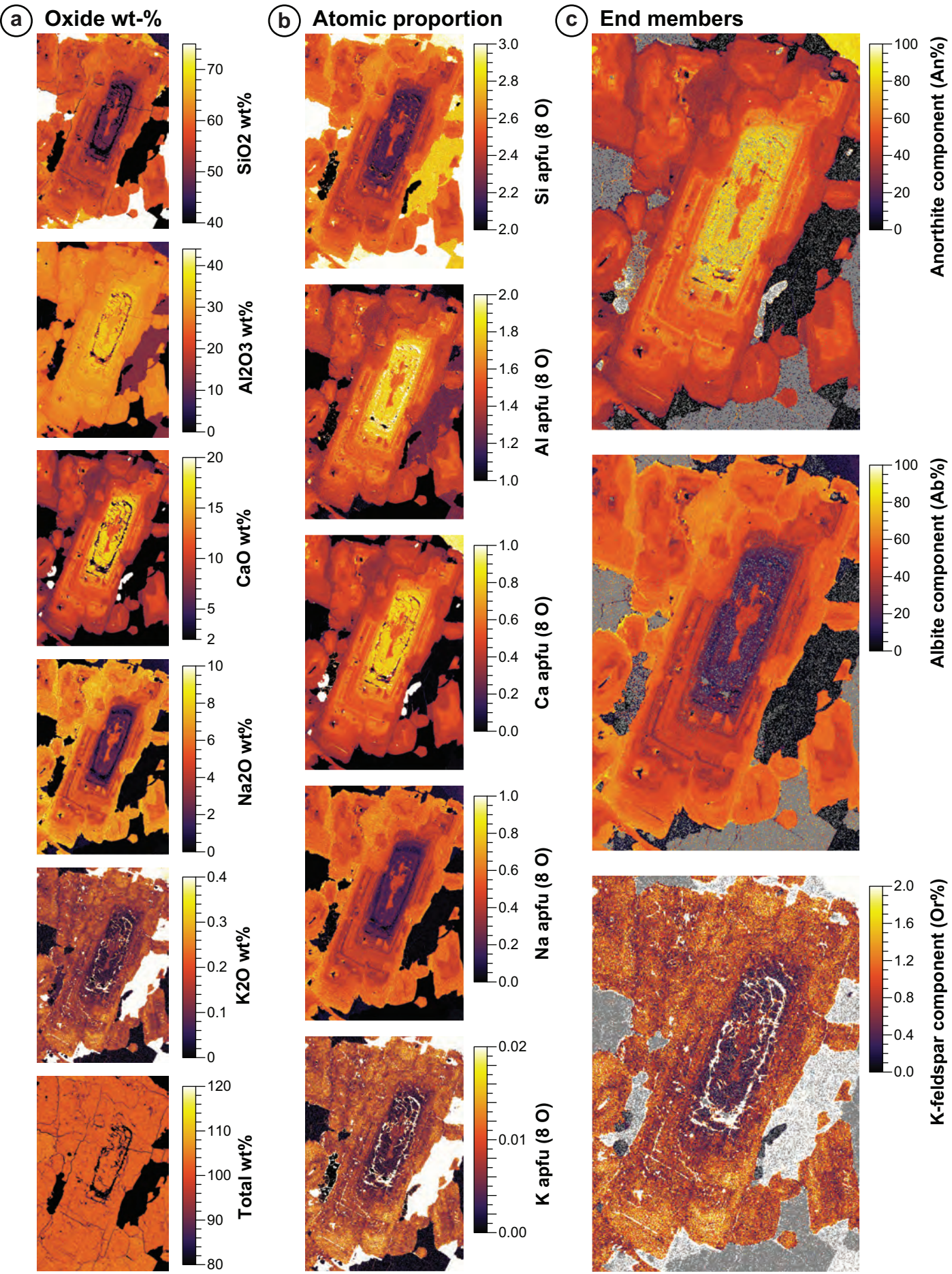
a
Oxide wt-%
SiO2 wt%
70
60
50
40
Al2O3 wt%
40
30
20
10
0
CaO wt%
20
15
10
5
2
Na2O wt%
10
8
6
4
2
0
K2O wt%
0.4
0.3
0.2
0.1
0
Total wt%
120
110
100
90
80
b
Atomic proportion
Si apfu (8 O)
3.0
2.8
2.6
2.4
2.2
2.0
Al apfu (8 O)
2.0
1.8
1.6
1.4
1.2
1.0
Ca apfu (8 O)
1.0
0.8
0.6
0.4
0.2
0.0
Na apfu (8 O)
1.0
0.8
0.6
0.4
0.2
0.0
K apfu (8 O)
0.02
0.01
0.00
c
End members
Anorthite component (An%)
100
80
60
40
20
0
Albite component (Ab%)
100
80
60
40
20
0
K-feldspar component (Or%)
2.0
1.6
1.2
0.8
0.4
0.0

Figure 4 *(continued)*

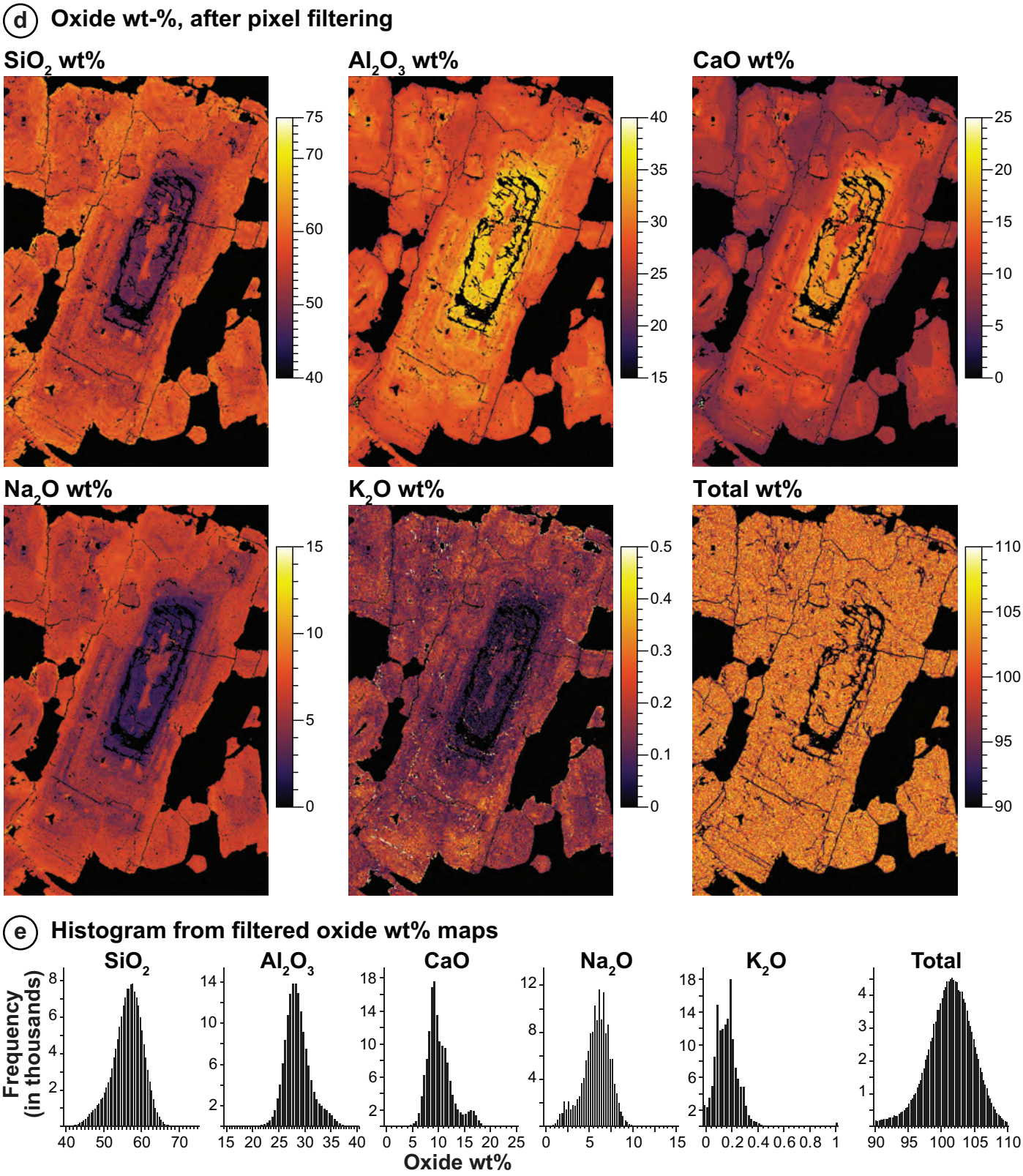

Figure 5

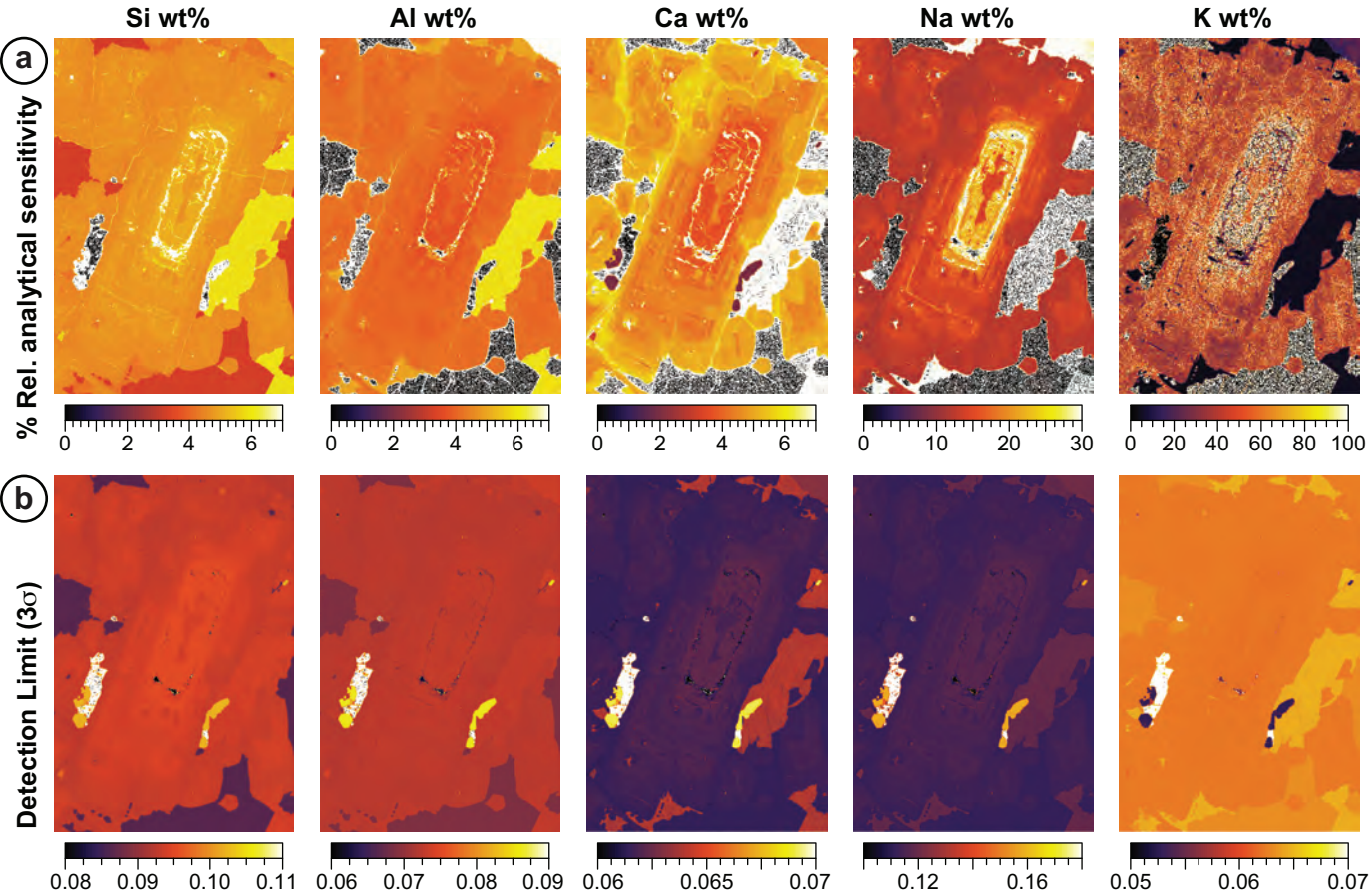
Si wt%
Al wt%
Ca wt%
Na wt%
K wt%
a
% Rel. analytical sensitivity
0 2 4 6
0 2 4 6
0 2 4 6
0 10 20 30
0 20 40 60 80 100
b
Detection Limit (3σ)
0.08 0.09 0.10 0.11
0.06 0.07 0.08 0.09
0.06 0.065 0.07
0.12 0.16
0.05 0.06 0.07

Figure 6

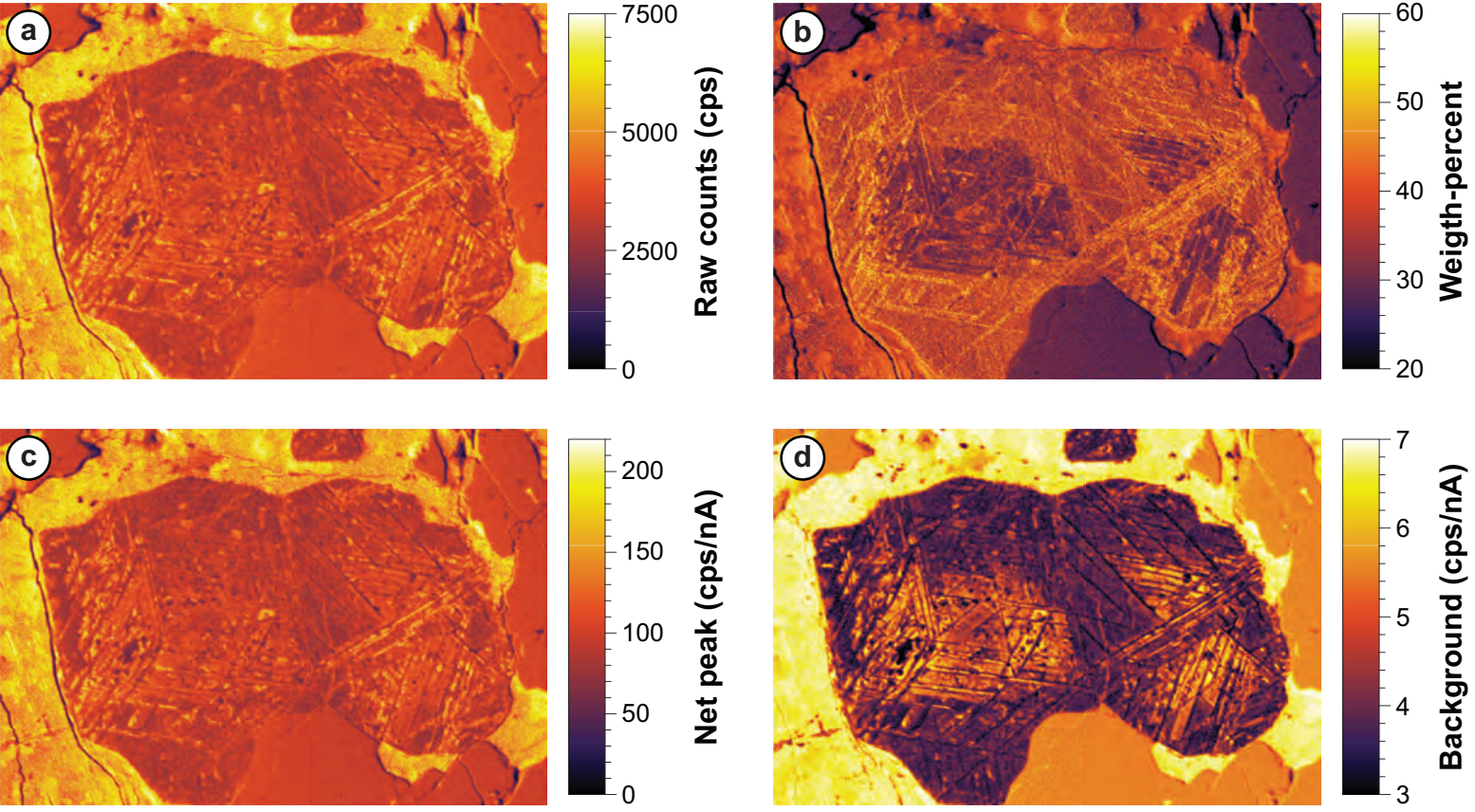
a
7500
5000
2500
0
Raw counts (cps)
b
60
50
40
30
20
Weigth-percent
c
200
150
100
50
0
Net peak (cps/nA)
d
7
6
5
4
3
Background (cps/nA)

Figure 7

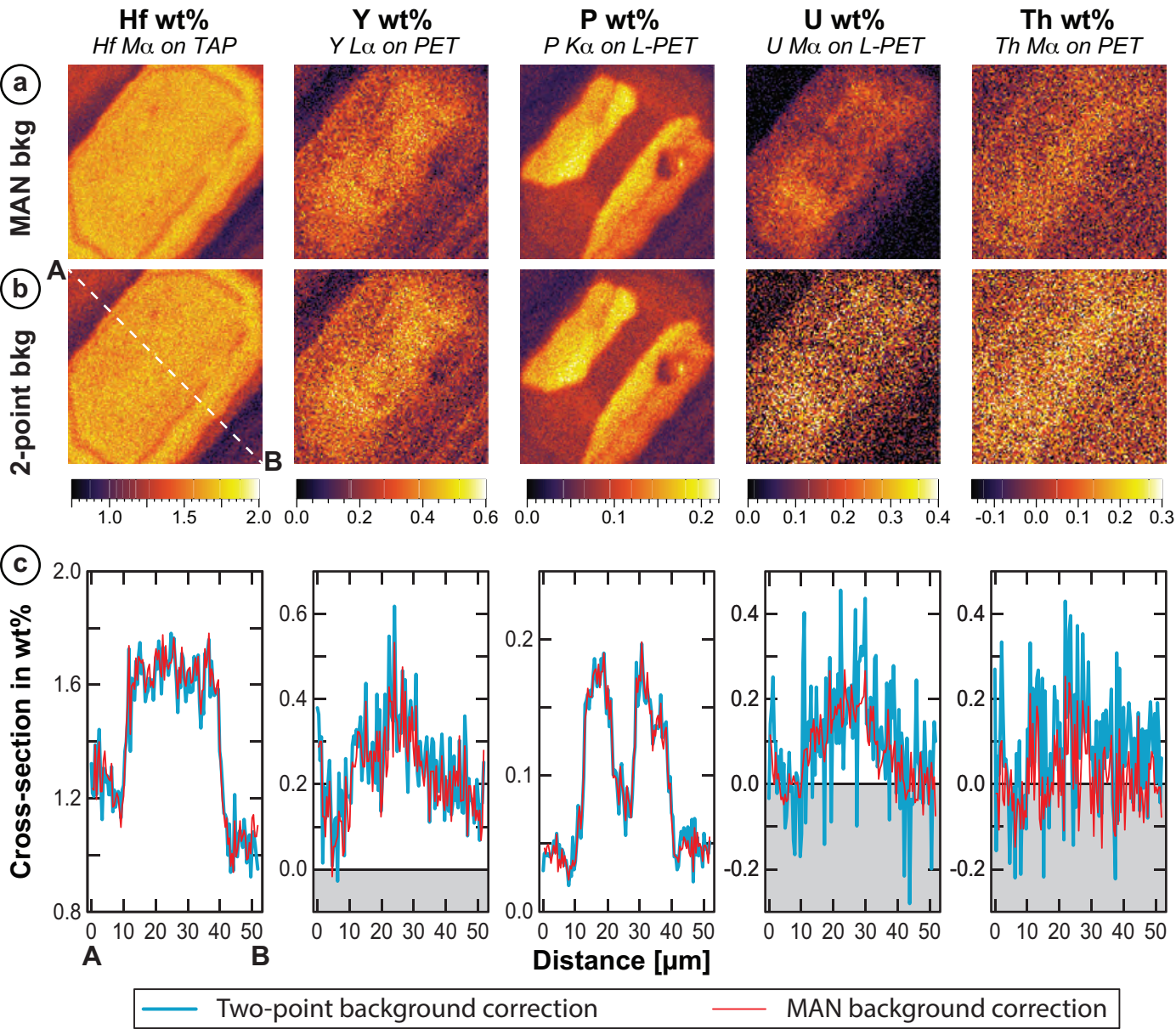
Hf wt%
Hf Mα on TAP
Y wt%
Y Lα on PET
P wt%
P Kα on L-PET
U wt%
U Mα on L-PET
Th wt%
Th Mα on PET
a
MAN bkg
b
2-point bkg
A
B
1.0 1.5 2.0
0.0 0.2 0.4 0.6
0.0 0.1 0.2
0.0 0.1 0.2 0.3 0.4
-0.1 0.0 0.1 0.2 0.3
c
Cross-section in wt%
2.0 1.6 1.2 0.8
0.6 0.4 0.2 0.0
0.2 0.1 0.0
0.4 0.2 0.0 -0.2
0.4 0.2 0.0 -0.2
0 10 20 30 40 50
A
B
Distance [µm]
Two-point background correction
MAN background correction

Figure 8

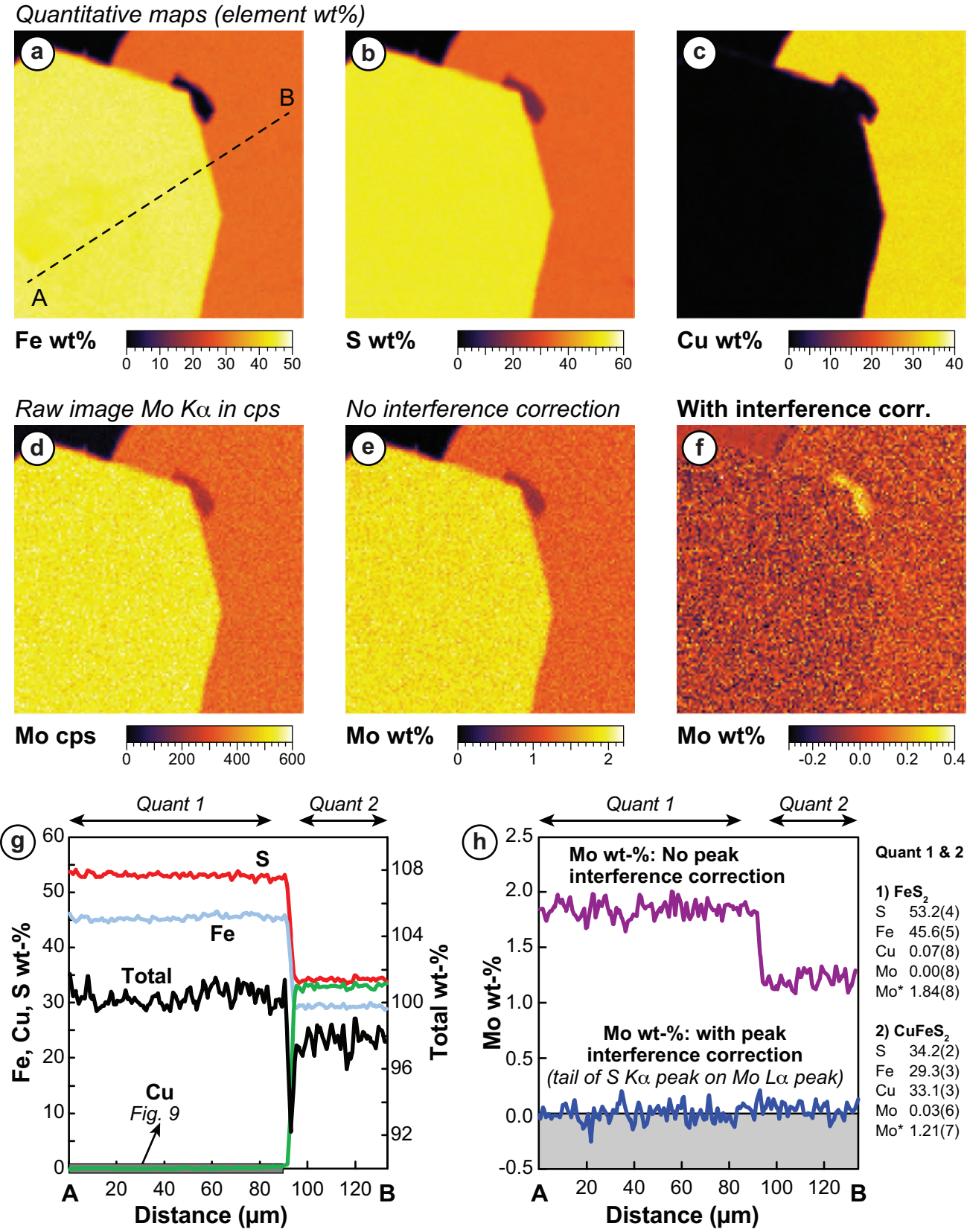
Quantitative maps (element wt%)
a
B
A
Fe wt%
0 10 20 30 40 50
b
S wt%
0 20 40 60
c
Cu wt%
0 10 20 30 40
Raw image Mo Kα in cps
d
Mo cps
0 200 400 600
No interference correction
e
Mo wt%
0 1 2
With interference corr.
f
Mo wt%
-0.2 0.0 0.2 0.4
g
Quant 1
Quant 2
S
Fe
Total
Cu
Fig. 9
Fe, Cu, S wt-%
Total wt-%
A
B
Distance (μm)
h
Quant 1
Quant 2
Mo wt-%: No peak interference correction
Mo wt-%: with peak interference correction
(tail of S Kα peak on Mo Lα peak)
Mo wt-%
A
B
Distance (μm)
Quant 1 & 2
1) FeS2
S 53.2(4)
Fe 45.6(5)
Cu 0.07(8)
Mo 0.00(8)
Mo* 1.84(8)
2) CuFeS2
S 34.2(2)
Fe 29.3(3)
Cu 33.1(3)
Mo 0.03(6)
Mo* 1.21(7)

Figure 9

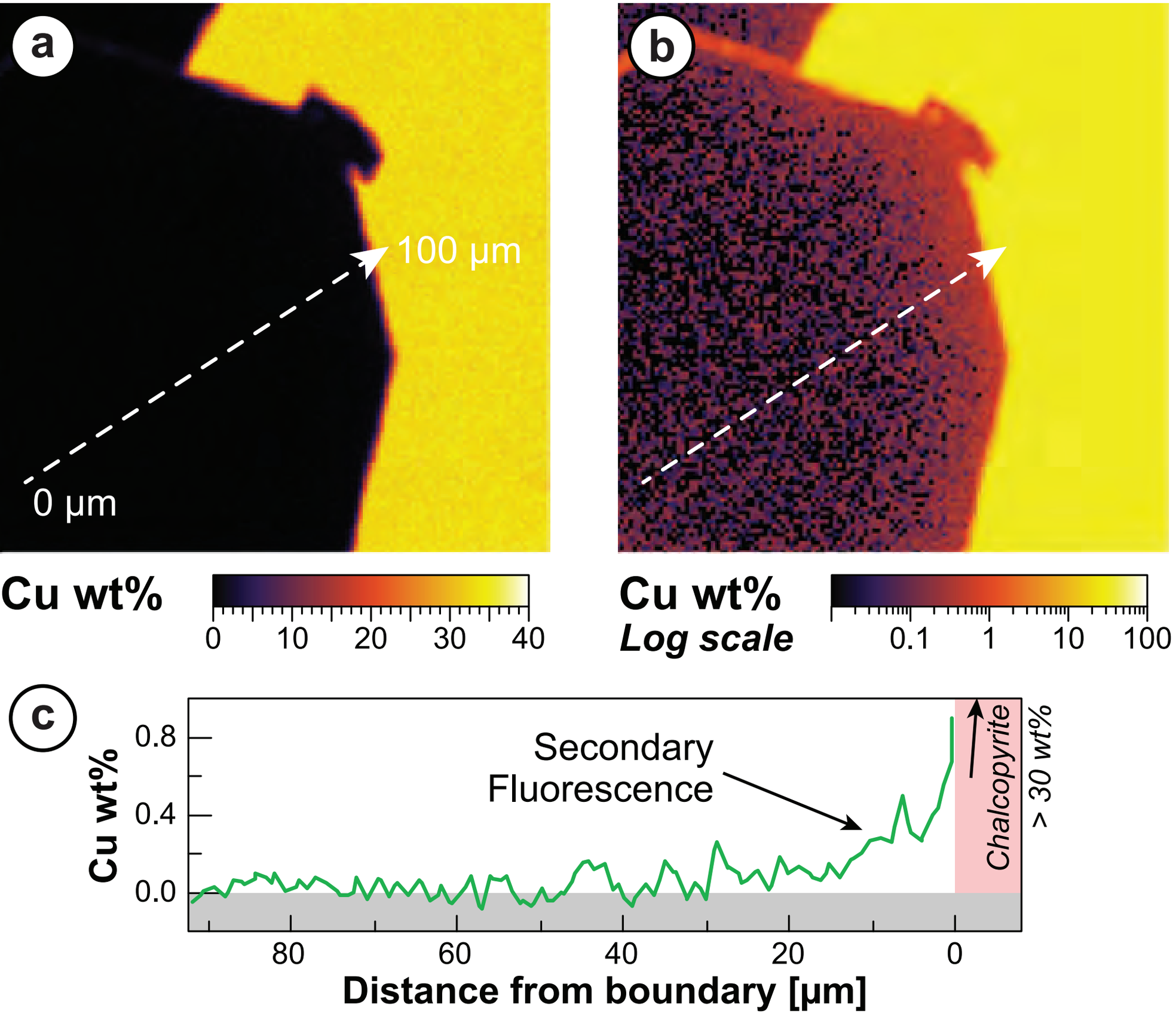
a
100 µm
0 µm
b
Cu wt%
0
10
20
30
40
Cu wt%
Log scale
0.1
1
10
100
c
Cu wt%
0.8
0.4
0.0
Secondary
Fluorescence
Chalcopyrite
> 30 wt%
80
60
40
20
0
Distance from boundary [µm]

Figure 10

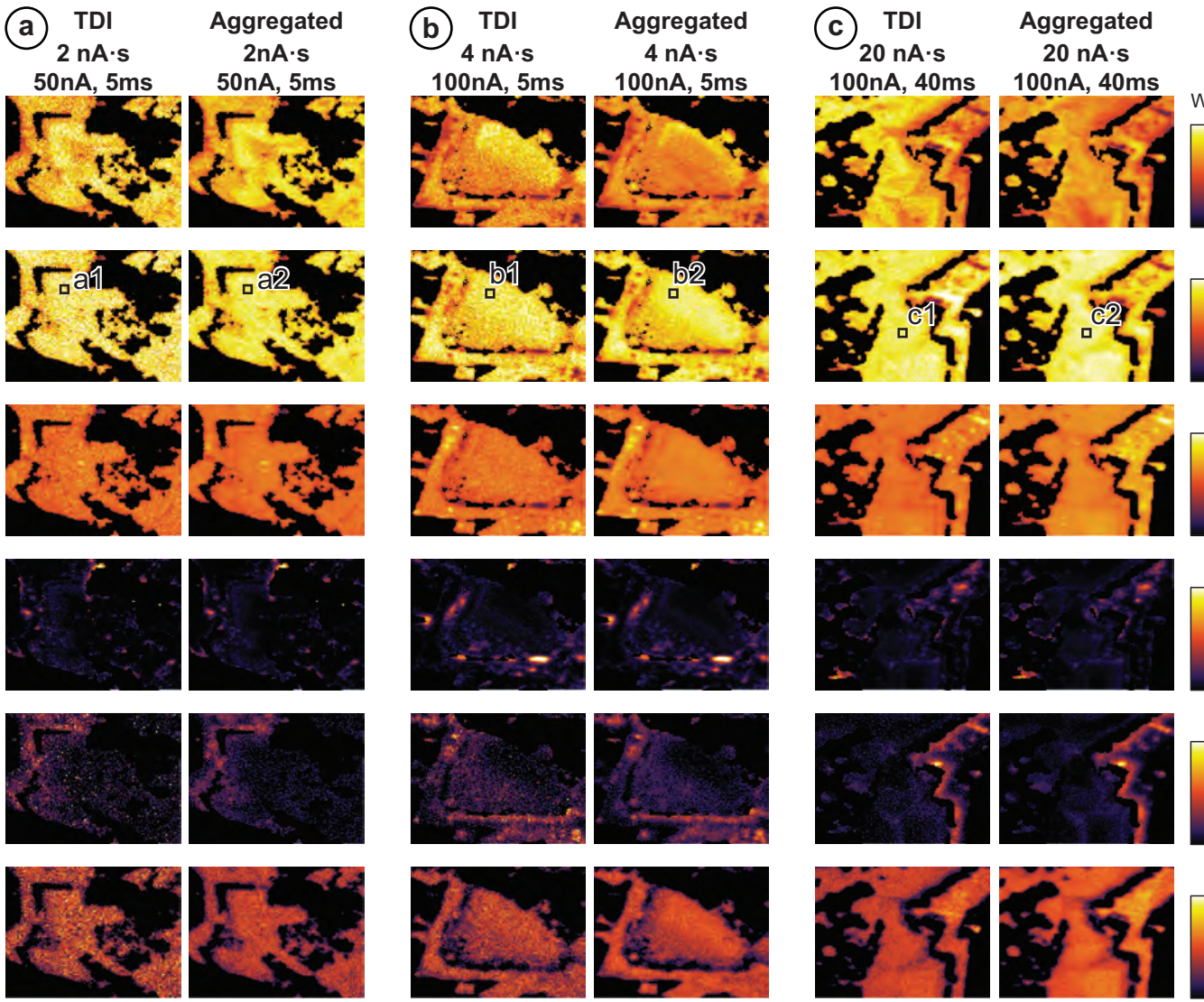

Any pixel with total below 80 wt% (e.g., other minerals, epoxy) is masked in black.

d 100-pixel averages (10x10 pixels; see location on SO_3 map)

	50 nA, 5 ms, 8 frames				100 nA, 5 ms, 8 frames				100 nA, 40 ms, 5 frames			
	a1 TDI	**a2 Agg.**	*FIRST*	*LAST*	**b1 TDI**	**b2 Agg.**	*FIRST*	*LAST*	**c1 TDI**	**c2 Agg.**	*FIRST*	*LAST*
K_2O	8.33*(12)*	8.24*(8)*	*8.32*	*8.16*	8.88*(9)*	7.16*(4)*	*8.94*	*6.18*	8.39*(6)*	7.12*(3)*	*8.44*	*6.49*
SO_3	33.0*(5)*	32.6*(2)*	*33.2*	*32.0*	32.5*(3)*	33.2*(1)*	*32.4*	*34.0*	32.91*(14)*	34.16*(10)*	*32.8*	*34.9*
Fe_2O_3	46.0*(4)*	45.5*(2)*	*45.5*	*45.6*	45.4*(3)*	47.8*(2)*	*45.1*	*49.7*	44.00*(14)*	48.08*(8)*	*44.7*	*51.4*
Al_2O_3	0.85*(7)*	0.79*(5)*	*0.84*	*0.75*	0.89*(6)*	0.87*(4)*	*0.83*	*0.88*	1.81*(6)*	1.92*(5)*	*1.85*	*2.00*
As_2O_5	0.18*(6)*	0.06*(1)*	*0.08*	*0.05*	0.05*(1)*	0.06*(1)*	*0.06*	*0.08*	0.12*(1)*	0.13*(1)*	*0.10*	*0.13*
*H_2O**	*11.48*	*11.46*	*11.48*	*11.55*	*11.07*	*11.03*	*11.04*	*10.98*	*11.57*	*11.39*	*11.55*	*11.25*
Total	**99.30**	**98.10**	***98.88***	***97.61***	**98.70**	**100.13**	***98.23***	***101.91***	**98.28**	**102.43**	***98.88***	***105.86***

** Calculated by stoichiometry: 6 H for 14 O.*

Figure 11

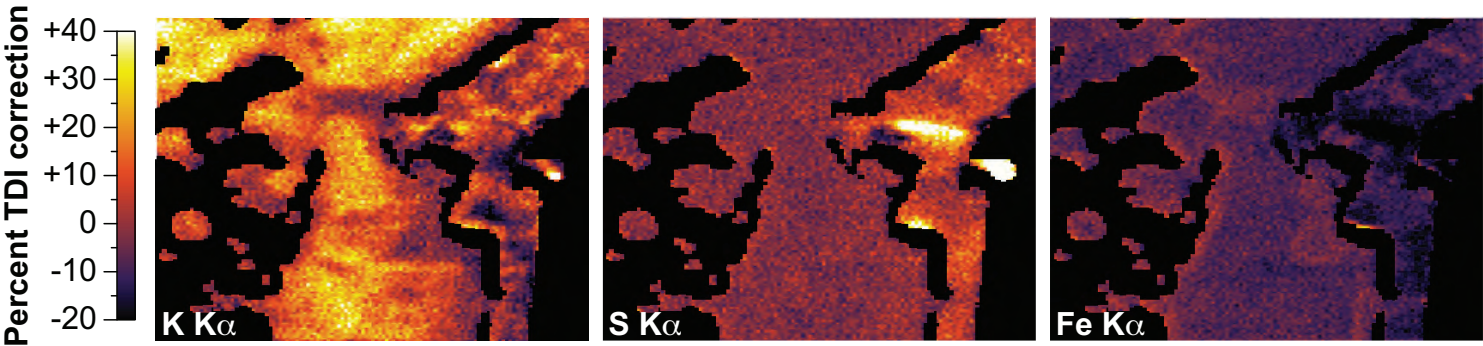

Mostly positive TDI correction

Mostly negative TDI correction

Figure 12

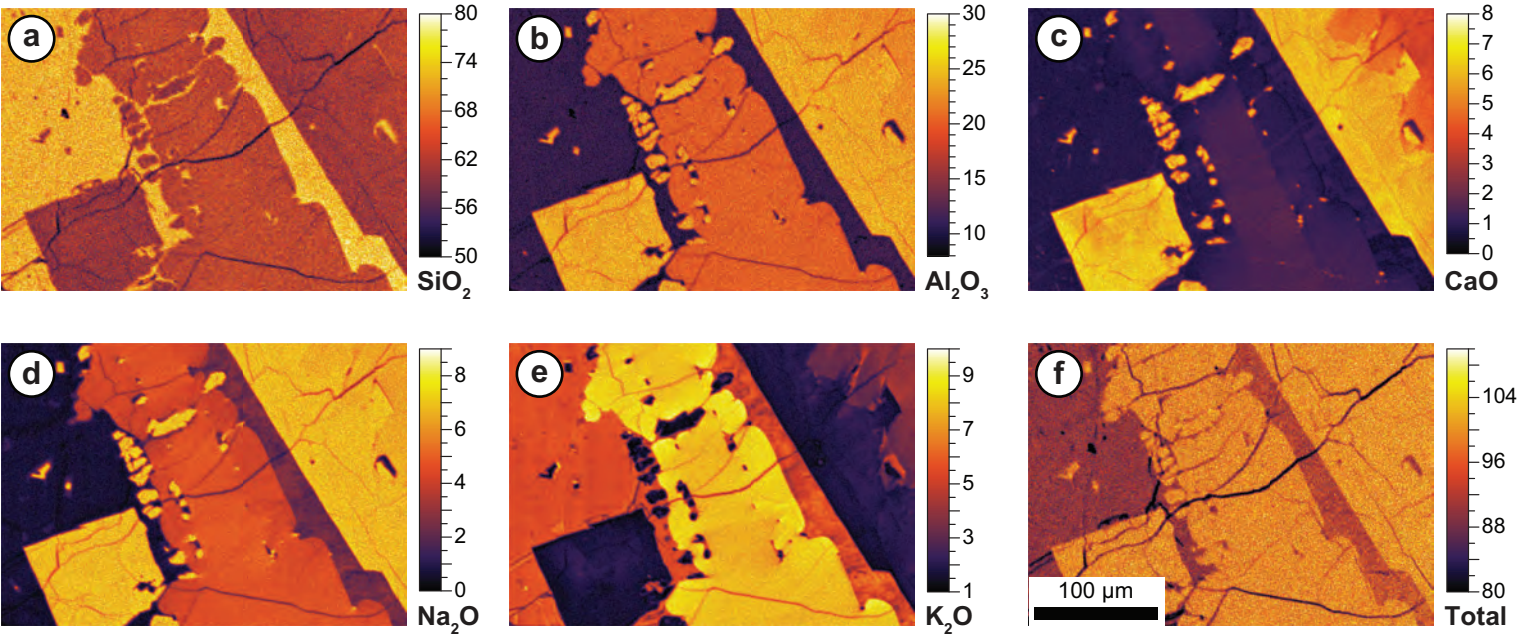

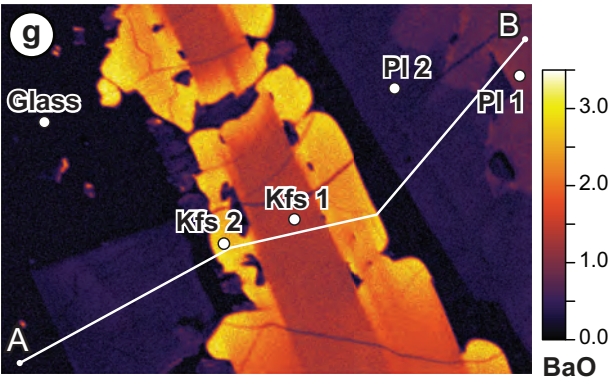

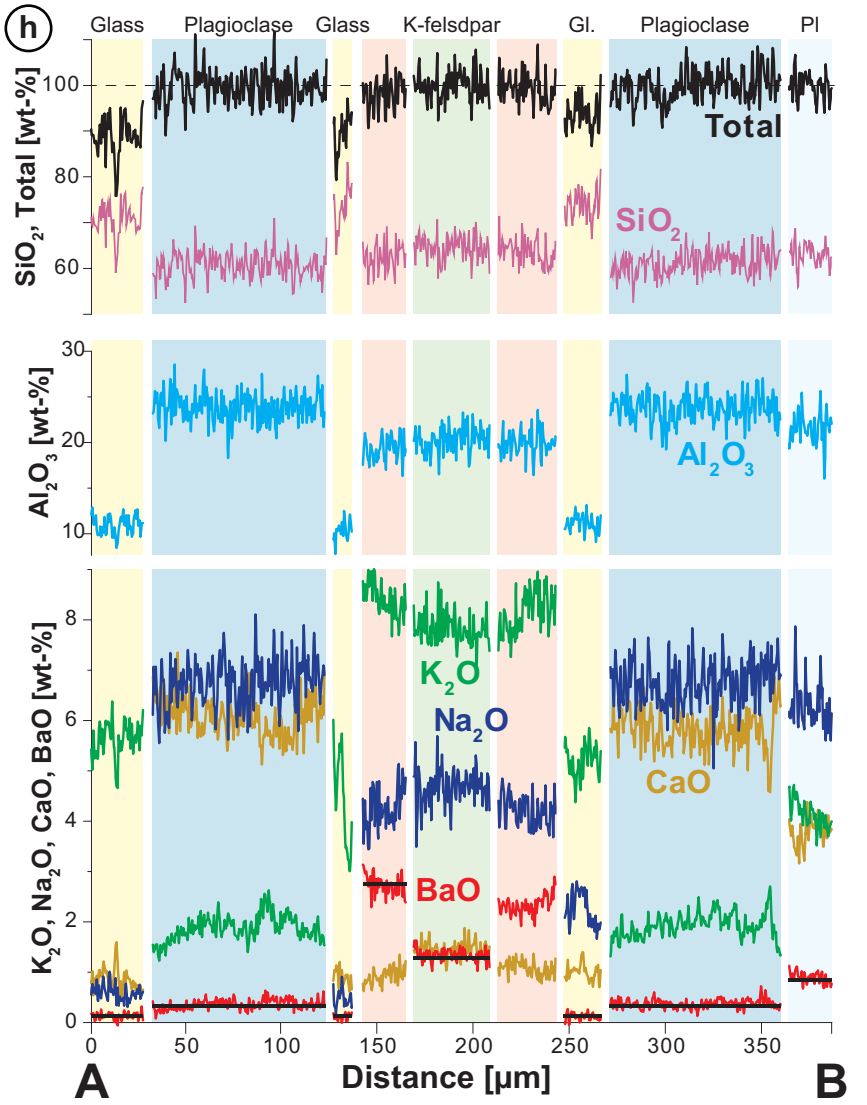

i Quantitative analysis point

	Kfs 1	Kfs 2	Pl 1	Pl 2	Glass
SiO_2	64.44	63.68	63.63	60.72	73.16
TiO_2	*0.04*	*0.04*	*0.03*	*0.02*	*0.29*
Al_2O_3	19.82	20.26	22.81	24.55	11.66
FeO	*0.18*	*0.19*	*0.24*	*0.35*	*2.47*
MnO	*0.00*	*-0.01*	*0.00*	*0.00*	*0.05*
MgO	*0.01*	*0.00*	*0.01*	*0.01*	*0.05*
CaO	1.42	0.89	3.71	6.12	0.78
SrO	*0.09*	*0.08*	*0.11*	*0.09*	*0.01*
BaO	1.28	2.75	0.83	0.32	0.12
Na_2O	4.80	4.31	6.22	6.67	2.17
K_2O	7.98	8.71	4.12	1.72	6.50
Total	100.06	100.91	101.72	100.59	97.26